Magnetic ordering in the layered Cr(II) oxide arsenides $Sr_2CrO_2Cr_2As_2$ and $Ba_2CrO_2Cr_2As_2$

Xiaoyu Xu,[1] Michael A. Jones,[1] Simon J Cassidy,[1] Pascal Manuel,[2] Fabio Orlandi,[2] Maria Batuk,[3] Joke Hadermann[3] and Simon J Clarke[1*]

[1]*Department of Chemistry, University of Oxford, Inorganic Chemistry Laboratory, South Parks Road, Oxford, OX1 3QR, UK.*

[2]*ISIS Facility, STFC Rutherford Appleton Laboratory, Harwell Oxford, Didcot OX11 0QX, United Kingdom*.

[3]*Electron Microscopy for Materials Science (EMAT), University of Antwerp, Groenenborgerlaan 171, B-2020 Antwerp, Belgium.*

email: simon.clarke@chem.ox.ac.uk

Abstract

$Sr_2CrO_2Cr_2As_2$ and $Ba_2CrO_2Cr_2As_2$ with Cr^{2+} ions in CrO_2 sheets and in CrAs layers crystallize with the $Sr_2Mn_3Sb_2O_2$ structure (space group *I*4/*mmm*, *Z* = 2) and lattice parameters *a* = 4.00800(2) Å, *c* = 18.8214(1) Å ($Sr_2CrO_2Cr_2As_2$) and *a* = 4.05506(2) Å, *c* = 20.5637(1) Å ($Ba_2CrO_2Cr_2As_2$) at room temperature. Powder neutron diffraction reveals checkerboard-type antiferromagnetic ordering of the Cr^{2+} ions in the arsenide layers below T_{N1_Sr}, of 600(10) K ($Sr_2CrO_2Cr_2As_2$) and T_{N1_Ba} 465(5) K ($Ba_2CrO_2Cr_2As_2$) with the moments initially directed perpendicular to the layers in both compounds. Checkerboard-type antiferromagnetic ordering of the Cr^{2+} ions in the oxide layer below 230(5) K for $Ba_2CrO_2Cr_2As_2$ occurs with these moments also perpendicular to the layers, consistent with the orientation preferences of d^4 moments in the two layers. In contrast, below 330(5) K in $Sr_2CrO_2Cr_2As_2$ the oxide layer Cr^{2+} moments are initially oriented in the CrO_2 plane, but on further cooling these moments rotate to become perpendicular to the CrO_2 planes, while the moments in the arsenide layers rotate by 90° with the moments on the two sublattices remaining orthogonal throughout [behavior recently reported independently by Liu *et al. Phys. Rev. B* **2018**, *98*, 134416]. In $Sr_2CrO_2Cr_2As_2$ electron diffraction and high resolution powder X-ray diffraction data show no evidence for a structural distortion that would allow the two Cr^{2+} sublattices to couple, but high resolution neutron powder diffraction data suggest a small incommensurability between the magnetic structure and the crystal structure, which may account for the coupling of the two sublattices and the observed spin reorientation. The saturation values of the Cr^{2+} moments in the CrO_2 layers (3.34(1) μ_B (for $Sr_2CrO_2Cr_2As_2$) and 3.30(1) μ_B (for $Ba_2CrO_2Cr_2As_2$)) are larger than those in the CrAs layers (2.68(1) μ_B for $Sr_2CrO_2Cr_2As_2$ and 2.298(8) μ_B for $Ba_2CrO_2Cr_2As_2$) reflecting greater covalency in the arsenide layers.

Keywords.

Antiferromagnet, spin-reorientation, oxide arsenide, chromium, oxypnictide

Introduction

Complex transition metal compounds containing oxide and the anion of a less electronegative element such as a chalcogen (*Ch*: S, Se, Te) or pnictogen (*Pn*: P, As, Sb, Bi) ion have enjoyed a resurgence since the discovery of high temperature superconductivity in layered iron arsenides and selenides. A common crystal structure adopted by quinary oxide chalcogenides and oxide pnictides is that of the $A_2Mn_3Pn_2O_2$ series (*A* = Sr, Ba; *Pn* = As, Sb, Bi) originally reported by Brechtel *et al.*,[1] extended to include the phosphide $Ba_2Mn_3P_2O_2$[2] and characterized by Brock *et al.*[3,4] In the structure, A_2MnO_2 layers containing MnO_2 square sheets are separated by anti-PbO-type Mn*Pn* layers with the transition metal ions in edge-shared $MnPn_4$ tetrahedra. This is shown for the title compounds, in which Cr replaces Mn, in Figure 1. The anti-PbO-type pnictide layers are found in superconducting iron arsenides and selenides and in the ZrCuSiAs[5,6] and $ThCr_2Si_2$ or $BaZn_2P_2$ structures.[7,8] Numerous transition metals and Zn may be incorporated into the oxide and chalcogenide or pnictide layers of these oxide chalcogenides and oxide pnictides,[9,10,11] with the cations of the less electronegative and less oxophilic elements preferentially incorporated into the chalcogenide or pnictide layers. With two very different transition metal environments in these compounds, the formulae may informatively be written as $A_2MnO_2Mn_2Pn_2$. We adopt this convention for the title compounds $Sr_2CrO_2Cr_2As_2$ and $Ba_2CrO_2Cr_2As_2$ and label the ions as Cr(1) in the oxide layer and Cr(2) in the pnictide layer as in the literature,[3,12,13] (Figure 1). The structural relationships between these and related compounds have been reviewed.[14,15,16]

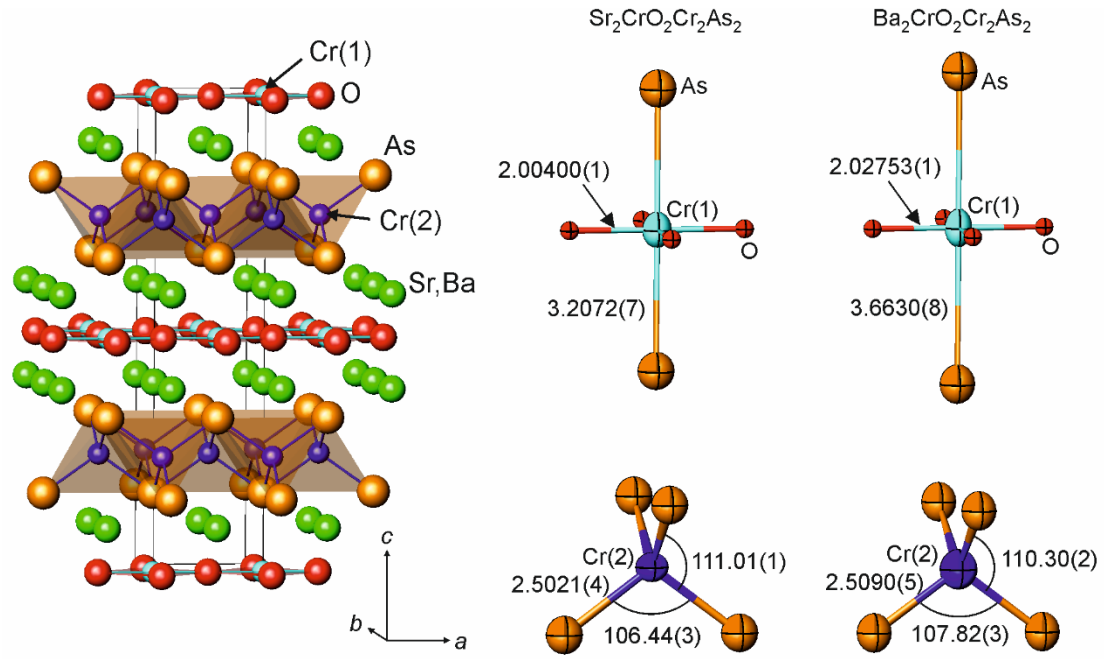

Figure 1. Crystal structure of $Sr_2CrO_2Cr_2As_2$ and $Ba_2CrO_2Cr_2As_2$ with the Cr(1) (oxide layer) and Cr(2) (arsenide layer) sites defined. The details show, to scale, the local coordinations around the Cr(1) and Cr(2) ions in the two compounds. 99% displacement ellipsoids derived from the ambient temperature I11 refinements are shown.

Compounds with Mn^{2+} ions in both oxide and pnictide layers have been described by Brock *et al.*[3,4] In $Sr_2MnO_2Mn_2As_2$ and $Sr_2MnO_2Mn_2Sb_2$ moments carried by the Mn ions in the pnictide layers order antiferromagnetically below 340 K and 300 K respectively with antiferromagnetic coupling of nearest neighbour moments which are directed perpendicular to the layers. A similar magnetic ordering scheme is found for Mn moments in $BaMn_2As_2$ below 625 K[17] and in *Ln*MnAsO (*Ln* = La, Ce, Nd, Pr) in the regime where only the Mn sublattice is magnetically ordered.[18,19,20] Brock *et al.* note the correlation between high ordering temperature and short Mn–Mn distance in the oxide pnictides and related compounds.[4] The manganese moments in the $[MnO_2]^{2-}$ layers of the oxide antimonide $Sr_2MnO_2Mn_2Sb_2$ also show antiferromagnetic coupling of nearest

neighbours below 65 K with these moments orthogonal to those in the antimonide layer (i.e. within the MnO_2 plane)[3] and the moments in the two layers behaving as independent magnetic systems.[21] In $Sr_2MnO_2Mn_2As_2$, $Sr_2MnO_2Zn_2As_2$ and $Ba_2MnO_2Zn_2As_2$ only short-range ordering of the MnO_2 layer magnetic moments was observed.[3,11,22]. $Sr_2MnO_2Mn_2As_2$,[22] $BaMn_2As_2$[23,24] and *Ln*MnAsO compounds (*Ln* = early lanthanide)[19,25] with similar MnAs layers are reported to be semiconducting.

Recently Jiang *et al.*[12] reported the synthesis of the Cr analogue $Sr_2CrO_2Cr_2As_2$ with Cr ions of nominal oxidation state +2 in both the distended octahedral CrO_4As_2 site in the oxide layers (Cr(1)) and in the tetrahedral $CrAs_4$ site (Cr(2)) in the arsenide layers. The compound $Sr_2CrFe_2As_2O_2$ has also been reported recently,[26] although the characterisation by X-ray diffraction does not allow the extent of Fe/Cr ordering to be determined in that case. Given the general difficulty of stabilising the Cr^{2+} oxidation state for Cr in oxides, Jiang *et al.*[12] entertained the reasonable possibility that in $Sr_2CrO_2Cr_2As_2$ the oxidation state was slightly greater than +2 in the oxide layer and slightly less than +2 in the arsenide layer. They also reported that a small level of contamination by a ferromagnetic chromium arsenide[27] impurity (T_C ~ 230 K) was very difficult to avoid, and that this hampered the characterisation of the intrinsic magnetic susceptibility, although there was evidence from magnetic susceptibility and heat capacity measurements for a magnetic ordering transition at 291 K. Compounds with similar CrAs layers are known and in LaCrAsO[28] and $BaCr_2As_2$[29] it is found that, unlike the Mn analogues, the compounds exhibit metallic resistivity, but with substantial localised moments on the Cr ions. An antiferromagnetically ordered moment of 1.57 μ_B was found at room temperature in LaCrAsO;[28] $BaCr_2As_2$ was predicted from first-principles calculations[29] to show ordering of localised Cr moments well above room temperature, and it was confirmed that this

compound indeed orders antiferromagnetically with T_N = 580(10) K.[30] Jiang *et al.*[12] found that $Sr_2CrO_2Cr_2As_2$ also exhibits itinerant behaviour and predicted that both the Cr(1) and Cr(2) sublattices would exhibit antiferromagnetic ordering using density-functional calculations within the generalised gradient approximation. In a parallel investigation to our own reported here, Liu *et al.*[13] recently described the temperature dependence of the magnetic ordering behaviour of $Sr_2CrO_2Cr_2As_2$ in which two independent Cr^{2+} sublattices ordering magnetically with different propagation vectors are somehow coupled, resulting in a spin-reorientation transition described below. Here we provide evidence from high resolution diffraction investigations for why $Sr_2CrO_2Cr_2As_2$ shows anomalous spin-reorientation behaviour. As a contrast we report additionally the new isostructural Ba analogue, $Ba_2CrO_2Cr_2As_2$, in which the two Cr^{2+} sublattices remain independent . We compare and contrast the behaviour with the Mn analogues and related compounds.

Experimental Methods

Synthesis. $Sr_2CrO_2Cr_2As_2$ was prepared on the 3g scale by reacting together SrO, Cr (Alfa 99.95%) and As (Alfa 99%) in stoichiometric amounts with the aid of a CsI flux. SrO was made by thermal decomposition of $SrCO_3$ (Alfa 99.994%) under dynamic vacuum (at 830°C for 16 hours followed by 1100°C for 4 hours). Stoichiometric amounts of the starting materials, were ground together with an equimolar amount of dry CsI (Alfa 99.998%) (i.e. molar ratio of "$Sr_2Cr_3As_2O_2$" : CsI = 1 : 1), and placed in an alumina crucible of mass ~ 30 g which was in turn placed in an evacuated silica ampule that had been pre-dried under vacuum to avoid hydrolysis of the products by water adsorbed on the surface of the ampule. The ampule was heated to 1100°C at a ramp rate of 2°C min^{-1}: the slow ramp rate ensuring that the volatile arsenic reacts before it attains a high vapour

pressure, then the temperature was maintained at 1100°C for 48 hours before the furnace was switched off and the ampule was allowed to cool to room temperature. After cooling, the black powder product remained in the alumina crucible, while the CsI flux was found to have mostly evaporated on to the surface of the silica tube. Consequently it was found to exist as a very minor contaminant in the product (~1 % by mass), and the samples were analysed without further attempts at purification, as washing had previously been found to introduce further contamination; the presence of CsI also aided temperature calibration in the PND experiment as described below. The use of the CsI flux reproducibly yielded the purest samples. Attempts to replicate the synthesis presented by Jiang *et al.*[12] (a flux-free ceramic synthesis at 900 °C from SrO, Cr and As) generally produced higher levels of contamination, and indeed, the recent work of Liu *et al.* confirms this.[13] In particular, in our syntheses, a persistent unidentified impurity was found with the most intense reflection at 2.79 Å (subsequently identified using electron microscopy as a new phase of formula $Sr_2Cr_2AsO_3$), although the use of higher firing temperatures of 1100 – 1200 °C did result in products approaching the purity obtained using the CsI flux. Because of the air-sensitivity of some of the reagents and possible air-sensitivity of the product, all manipulations, and storage of the samples were carried out in an argon-filled glove box. The characterisation was carried out on two 3 g samples (referred to as sample 1 and sample 2 in what follows). A polycrystalline sample of $Ba_2CrO_2Cr_2As_2$ was prepared by a solid-state-reaction using BaO (Aldrich 99.99%), Cr (Alfa 99.95%) and As (Alfa 99%) as starting materials in stoichiometric amounts. A pellet of the ground mixtures of the starting materials was placed in an Al_2O_3 crucible which was then sealed inside an evacuated pre-dried silica ampule. Firstly, the sample was heated to 800°C for 24 h at a slow rate of 2 °C/min, so that the As was reacted completely before it reached a high vapor pressure in the tube (the boiling point of As is 613 °C).[1] The mixture was then

reground for homogenization, pressed into a pellet, heated to 1200 °C at 10 °C min^{-1} and sintered at this temperature for 4 h followed by quenching into ice/water.

Diffraction measurements.

Powder X-ray Diffraction (PXRD) measurements were performed using the instrument I11 at the Diamond Light Source Ltd, UK with 0.826 Å X-rays (calibrated using a Si standard before each series of experiments).[31] High resolution diffraction patterns were collected on both samples at ambient temperature and at 100 K for $Sr_2CrO_2Cr_2As_2$ using the multi-analyzer crystal (MAC) detector of this instrument. Variable temperature PXRD patterns for $Sr_2CrO_2Cr_2As_2$ were obtained every 24 seconds using the MYTHEN position sensitive detector (PSD). Three such measurements were made: on cooling in a nitrogen cryostream between 290 and 100 K at a rate of 6 K min^{-1} and on warming in the cryostream between 250 and 400 K at 6 K min^{-1}, and on warming using a hot air blower between 300 and 673 K at 6 K min^{-1}. Powder Neutron Diffraction (PND) measurements were performed on both compounds using the WISH diffractometer[32] at the ISIS Facility, UK. For $Sr_2CrO_2Cr_2As_2$, samples 1 and 2 were contained inside 6 mm diameter vanadium cylinders. Sample 2 was measured only at ambient temperature and sample 1 was measured in the temperature range 1.5 K – 320 K in a helium cryostat, and separately in the range from room temperature to 623 K in a resistance furnace. Cadmium metal was used to mask the steel part of the sample container below room temperature, while gadolinium foil was used for the same purpose above RT. For $Ba_2CrO_2Cr_2As_2$, the sample was contained in a 6 mm vanadium cylinder with a gadolinium foil mask and measured in a closed cycle refrigerator equipped with a heating stage insert that enabled measurements on warming from ambient temperature to 600 K, followed by measurement on cooling to 5.5 K. Rietveld refinements of the crystal and magnetic

structures and model-independent Pawley-type fits against powder diffraction data were carried out using Topas Academic Version 5.[33] The web-based software ISODISTORT,[34] was used to aid the deduction of the magnetic models prior to Rietveld refinement.

Transmission Electron Microscopy

Electron diffraction (ED) patterns on $Sr_2CrO_2Cr_2As_2$ (sample 1) were acquired on a Philips CM20 transmission electron microscope operated at 200 kV at room temperature and at ~-170°C (following *in situ* cooling). High angle annular dark field (HAADF) scanning transmission electron microscopy (STEM) images were acquired using a FEI Titan 80-300 "cubed" microscope operated at 300 kV. A specimen for the TEM study was prepared by grinding the material under ethanol and depositing a few drops of the suspension onto a copper TEM grid covered by a holey carbon layer. The specimen was prepared in air.

Magnetometry

All measurements used a Quantum Design MPMS-XL SQUID magnetometer. For both $Sr_2CrO_2Cr_2As_2$ and $Ba_2CrO_2Cr_2As_2$ the susceptibility was determined by measuring the magnetization as a function of temperature on warming from 2 to 320 K after cooling both in zero applied field (zero-field cooled (ZFC)), and then in the measuring field (field cooled (FC)) of 50 mT ($Sr_2CrO_2Cr_2As_2$) or 100 mT ($Ba_2CrO_2Cr_2As_2$). Magnetization isotherms ($-5 \leq \mu_0 H / \mathrm{T} \leq 5$) were measured after cooling the sample from 300 K to the measurement temperature in a 5 T field. For these measurements at ambient temperature or below, samples of about 30 mg in mass were contained in gelatin capsules. Further measurements on both $Sr_2CrO_2Cr_2As_2$ and $Ba_2CrO_2Cr_2As_2$ were made in the range $300 \leq T / \mathrm{K} \leq 650$ using the furnace insert for the MPMS-XL magnetometer: the fresh samples

was measured on warming (ZFC) and on cooling (FC) in an applied field of 0.5 T. For these measurements the samples were contained in thin-walled silica ampules.

Results.

Synthesis and crystal structure refinement. For $Sr_2CrO_2Cr_2As_2$ the synthesis using the CsI flux route produced the highest quality samples according to the laboratory PXRD patterns. Rietveld analysis of the synchrotron PXRD data taken at ambient temperature and 100 K (Figure 2(a)) and PND data on sample 1 above the temperature where magnetic Bragg peaks are evident (see below) (Figure 2(b)) revealed small amounts of crystalline impurity phases which we have not been able to entirely eliminate, but all peaks were accounted for in the refinements. The diffraction measurements confirmed the model of Jiang *et al.*[12] and the refined structural parameters are presented in Table 1. Jiang *et al.* found that "*nearly single-phase samples could be prepared only by a small deviation of stoichiometry with 2-5% oxygen deficiency"* implying a possible degree of non-stoichiometry, however we tested this and found no evidence for oxygen deficiency from the synthesis nor from the refinements against PND data and speculate that additional oxygen to compensate for the deficiency introduced by Jiang *et al.*[12] could arise from the silica tubes. We also found no variation between samples of $Sr_2CrO_2Cr_2As_2$ outside the variation expected from making independent measurements of different samples (see Table 4). $Ba_2CrO_2Cr_2As_2$ was successfully synthesised only when high firing temperatures were used. The sample was contaminated by a significant amount of Cr_2As impurity, some $BaCr_2As_2$ and the diffraction pattern also contained some unindexed reflections which we presume arise from an as-yet unidentified Ba-containing impurity. In this case also there was no evidence from the refinements for bulk non-stoichiometry in the main phase. The refinement results against ambient temperature

synchrotron PXRD data and high temperature (above the magnetic ordering transitions) PND data for sample 1 of $Sr_2CrO_2Cr_2As_2$ and the sample of $Ba_2CrO_2Cr_2As_2$ are given in Tables 1-3 and Figure 2. See also Tables S1-S6 and Figures S3-S4.

Table 1 Refinement results for $Sr_2CrO_2Cr_2As_2$ (sample 1); and $Ba_2CrO_2Cr_2As_2$. Fits shown in Figure 2.

Compound	$Sr_2CrO_2Cr_2As_2$		$Ba_2CrO_2Cr_2As_2$	
Instrument	I11	WISH	I11	WISH
Radiation	X-ray	Neutron	X-ray	Neutron
Wavelength (Å)	0.825901	white beam	0.82606	white beam
Temperature (K)	298	623	298	473
R_{wp} (%)	7.90	3.51	8.05	3.58
Space group	*I*4/*mmm*	*I*4/*mmm*	*I*4/*mmm*	*I*4/*mmm*
a (Å)	4.00800(2)	4.03128(7)	4.05506(2)	4.07085(2)
c (Å)	18.8214(1)	19.0399(4)	20.5637(1)	20.5893(2)
V (Å^3)	302.347(4)	309.42(1)	338.140(4)	337.67(3)
ρ (g cm^{-3})	5.63573(8)	5.5069(2)	6.01558(7)	5.96161(8)
Cr(1)–O (Å) [4]	2.00400(1)	2.01564(4)	2.02753(1)	2.03542(0)
Cr(1)–As (Å) [2]	3.2072(7)	3.2391(6)	3.6630(8)	3.6793(9)
Cr(2)–As (Å) [4]	2.5021(4)	2.5251(3)	2.5090(5)	2.5096(5)
Sr/Ba–O (Å) [4]	2.5964(5)	2.6228(4)	2.7351(3)	2.7408(7)
Sr/Ba–As (Å) [4]	3.2333(5)	3.2499(4)	3.4001(5)	3.4184(8)
As–Cr–As (°) [2]	106.44(3)	105.93(2)	107.82(3)	108.40(4)
As–Cr–As (°) [4]	111.01(1)	111.27(1)	110.302(15)	110.010(16)

Table 2 structural parameters for $Sr_2CrO_2Cr_2As_2$ from Rietveld refinement against I11 RT data

atom	site	*x*	*y*	*z*	U_{11} /U_{22} (Å^2)[a]	U_{33} (Å^2)
Sr	4e	0	0	0.41229(4)	0.0107(3)	0.0133(5)
Cr(1)	2a	0	0	0	0.0098(5)	0.015(1)
Cr(2)	4d	0	0.5	0.25	0.0126(4)	0.0098(6)
As	4e	0	0	0.17040(4)	0.0155(3)	0.0165(5)
O	4c	0	0.5	0	0.004(1)[b]	0.004(1)[b]

[a] $U_{11} = U_{22}$ by symmetry for sites refined anisotropically.

[b] O atoms refined isotropically

Table 3 structural parameters for $Ba_2CrO_2Cr_2As_2$ from Rietveld refinement against I11 RT data.

atom	site	*x*	*y*	*z*	U_{11} / U_{22} (Å^2)[a]	U_{33} (Å^2)
Ba	4*e*	0	0	0.41073(2)	0.0149(2)	0.0161(3)
Cr(1)	2*a*	0	0	0	0.0090(6)	0.018(1)
Cr(2)	4*d*	0	0.5	0.25	0.0176(5)	0.0199(8)
As	4*e*	0	0	0.17813(4)	0.0152(4)	0.0189(6)
O	4*c*	0	0.5	0	0.012(2)[b]	0.012(2)[b]

[a] $U_{11} = U_{22}$ by symmetry for sites refined anisotropically.
[b] O atoms refined isotropically.

Table 4. Comparison of $Sr_2CrO_2Cr_2As_2$ samples from ambient temperature synchrotron PXRD data.

Sample	*a* (Å)	*c* (Å)	*c*/*a*	V (Å^3)	*z*(Sr)	*z*(As)	χ^2	R_{wp} (%)
Jiang *et al.*[12]	4.0079(1)	18.8298(3)	4.6982(2)	302.47(1)	0.4123(1)	0.1701(1)	3.0	7.3
Sample 1[a]	4.00800(2)	18.8214(1)	4.69596(4)	302.347(4)	0.41229(3)	0.17040(3)	2.22	7.90
Sample 2[b]	4.00856(8)	18.8268(4)	4.6967(1)	302.52(1)	0.41251(3)	0.17056(3)	5.37	1.72

[a]MAC detector
[b]MYTHEN PSD detector

Table 4 shows that there is little evidence, from the lattice and structural parameters, of compositional variation between the samples of $Sr_2CrO_2Cr_2As_2$, which might have arisen from the slight oxygen non-stoichiometry proposed by Jiang *et al.*[12] Refinement of the fractional oxygen occupancy in $Sr_2CrO_2Cr_2As_2$ using PND data at 623 K produced a refined value of 1.017(3) which we deem to indicate full occupancy, so there was no indication of the possible oxygen deficiency proposed by Jiang *et al.*[12] Because of the low atomic number of O, the refinements against synchrotron data were relatively insensitive to the fractional occupancy of the site and occupancies ranging between 0.92 and 1.08 were obtained depending on whether the form factor for O^{2-} or neutral O respectively was used. In the PND experiment O makes a relatively larger contribution to the scattering and the scattering length is independent of the chemistry of the element.

A similar analysis for $Ba_2CrO_2Cr_2As_2$ in which Rietveld refinements against both X-ray and neutron powder diffraction data were used to investigate the possibility of deficiencies on the oxide site and the Cr site in the arsenide layer concluded that this compound too was stoichiometric within the experimental uncertainty of 1-2 %.

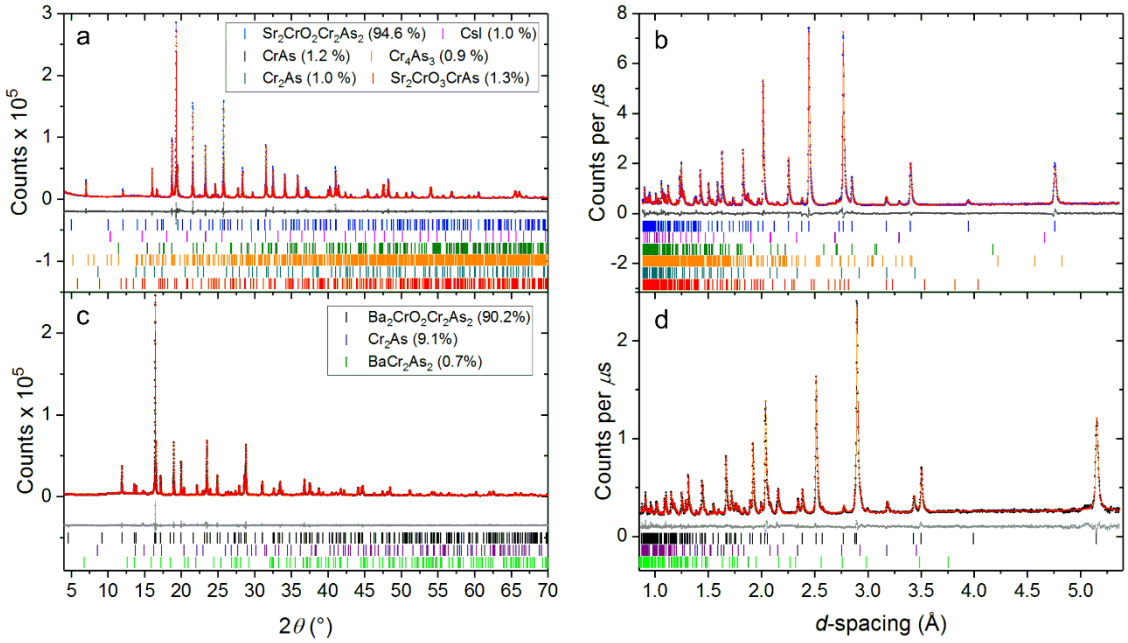

Figure 2. Rietveld refinements of the nuclear structure of $Sr_2CrO_2Cr_2As_2$ against synchrotron PXRD data (I11) collected at room temperature (a) and PND data (WISH) at 623K (b). (c) and (d) show equivalent Rietveld refinements for $Ba_2CrO_2Cr_2As_2$: synchrotron PXRD data at room temperature (c) and PND data at 473 K(d). Data from the 2θ = 120° data bank of WISH is presented in (b) and (d).

Magnetic susceptibility. Magnetic susceptibility measurements below room temperature for $Sr_2CrO_2Cr_2As_2$ were similar to those reported by Jiang *et al.*[12] and were dominated by a small amount of ferromagnetic chromium arsenide impurity which we were not able to eliminate in the syntheses. It is clearly extrinsic to the main phase because the magnetization varied in magnitude from sample to sample. The $Ba_2CrO_2Cr_2As_2$ sample was evidently free from this impurity, and showed no signs of magnetic transitions below room temperature (Figure S11(a)). SQUID magnetometry measurements above room temperature (see Figure S11(b) for $Ba_2CrO_2Cr_2As_2$) were noisy on account of the

experimental configuration; we found that there were no clear features associated with magnetic ordering in these susceptibility measurements, so we use the analysis of the PND data to discuss the ordering phenomena.

Magnetic ordering. PND measurements on $Sr_2CrO_2Cr_2As_2$ revealed that there were intense diffraction peaks present at ambient temperature which were not predicted by the structural model although these diminished to the background level on warming the sample above 600(10) K and were most intense at long *d*-spacings, suggesting that they arose from long range magnetic ordering. Hence we report above the nuclear-only crystal structure refinement above from PND data collected at 623 K (Figure 2, Table 1). Measurements below a Neél temperature estimated in our measurements as 600(10) K (similar within the uncertainty to the 590.3(7) K determined by Liu *et al.*[13]) down to 1.5 K revealed dramatic changes in the relative intensities of these reflections around room temperature as shown in Figure 3(a). Similar measurements on $Ba_2CrO_2Cr_2As_2$ revealed similar sets of magnetic reflections evident in the neutron diffractograms collected below 473(10) K (Figure 3(b)). The quantitative thermal evolution of the reflections in the two compounds are quite different as we discuss below.

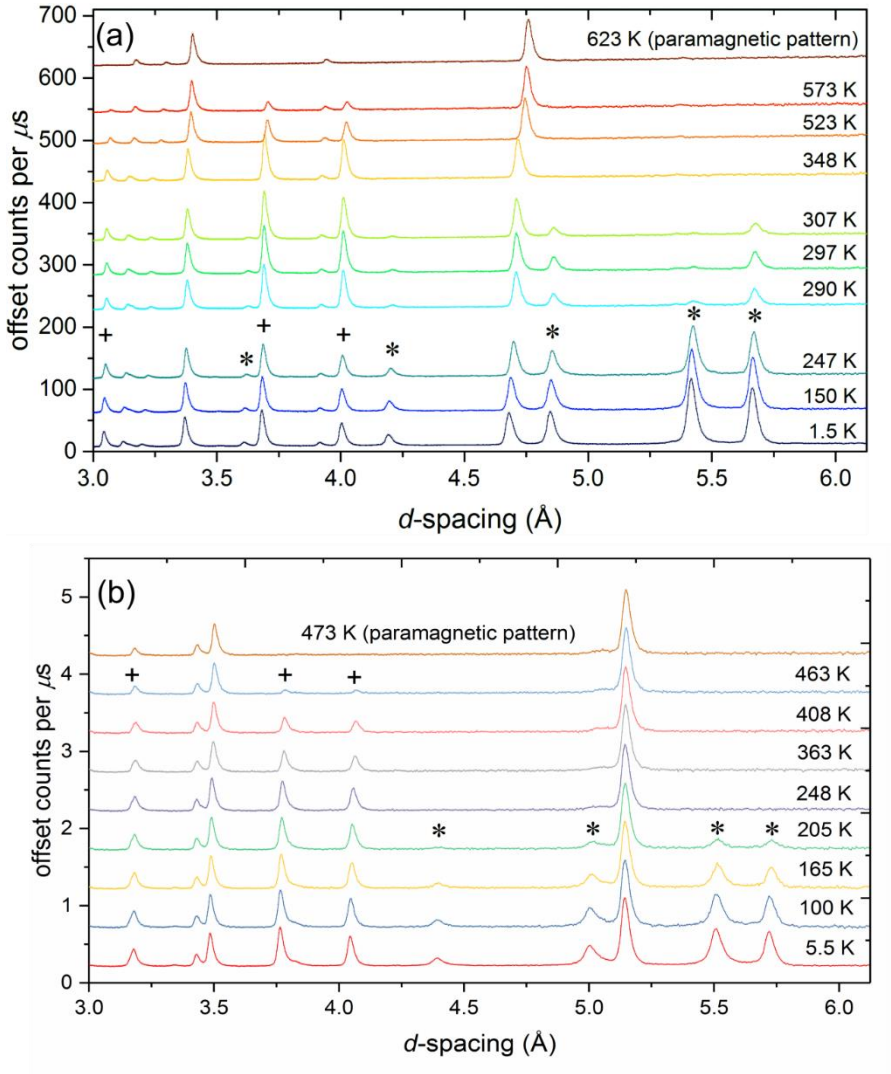

Figure 3. (a) WISH PND data of $Sr_2CrO_2Cr_2As_2$ in the range 1.5 to 623 K (combination of banks 3 and 8 at $2\theta = 90°$). The data have been offset along the vertical axis for clarity. Several magnetic peaks marked with (*) and (+) are present at 1.5 K, which all persist on warming to 247 K. At 290K the peaks marked (*) have greatly diminished in intensity and are absent at 348 K. However, the peaks marked (+) increase in intensity over the same range. Above 348 K the magnetic peaks marked (+) diminish in intensity and are completely absent in the pattern collected at 623 K. The changes in intensity result from the onset of ordering of the moments on the two Cr sublattices occurring at different temperatures, and from a spin-reorientation transition as described in the main text. (b) Analogous data for $Ba_2CrO_2Cr_2As_2$ with the magnetic Bragg peaks labelled in a similar way. For further description of the similarities and differences in the two compounds, see text.

Between 598 K and 348 K in $Sr_2CrO_2Cr_2As_2$, and at lower temperatures, between 473 K and 233 K, in $Ba_2CrO_2Cr_2As_2$, the magnetic Bragg peaks (peaks marked "+" in Figure 3) were modelled successfully by just introducing long range ordering of the magnetic moments of the Cr(2) ions in the CrAs layers. Nearest-neighbour moments were coupled

antiferromagnetically in a checkerboard fashion with the moments directed along the *c*-direction perpendicular to the planes in both compounds. The ordering scheme is similar to that displayed by the Mn analogues with As or Sb pnictide ions[3] and to the compounds LaCrAsO[28] and $BaCr_2As_2$[30] with similar CrAs layers, except that the Cr(2) moments in adjacent layers related by the vector ***c***/2 are aligned parallel in $Sr_2CrO_2Cr_2As_2$ and $Ba_2CrO_2Cr_2As_2$ rather than antiparallel. In this high temperature regime the moments carried by the Cr(1) ions in the CrO_2 layers were found not to contribute to the magnetic Bragg peaks. Figure 4(a) shows the refinement and the magnetic model for $Sr_2CrO_2Cr_2As_2$ at 348 K after the reflections marked with (+) symbols in Figure 3(a) have grown significantly in intensity. Figure 5(a) shows the refinement at a similar stage for $Ba_2CrO_2Cr_2As_2$. In this high temperature regime, the magnetic structure described by the Cr(2) moments has a k = (1 1 1) propagation vector and can be described using a primitive tetragonal cell with lattice parameters $a_{nucl} \times a_{nucl} \times c_{nucl}/2$ relative to the nuclear cell.

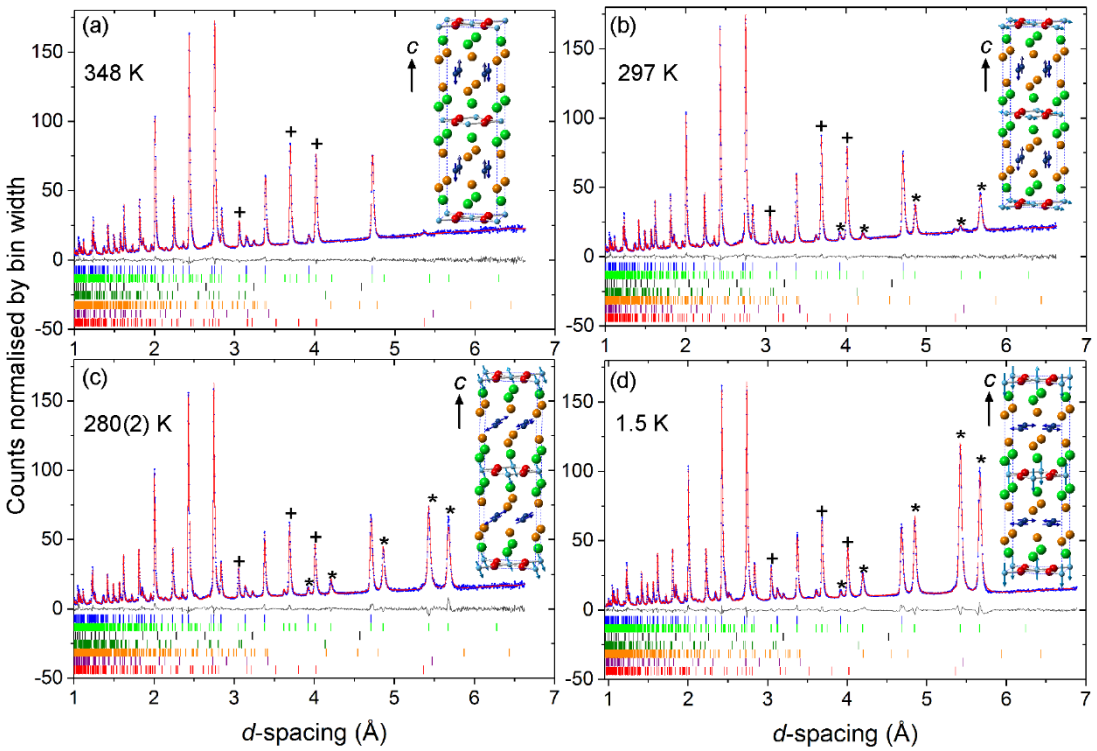

Figure 4. Rietveld refinements against PND data for $Sr_2CrO_2Cr_2As_2$ from WISH bank 3/8 (2θ = 90°). The insets depict the ordering and relative magnitudes and orientations of the magnetic moments at the given temperature. (a) At 348K one set of magnetic peaks are observed due to ordering of the Cr(2) sublattice (dark blue), the most prominent of which are labelled with a cross (+). χ^2 = 0.75, R_{wp} = 3.62. (b) At 297(1) K an additional set of magnetic peaks appears due to ordering of the Cr(1) sublattice (light blue), labelled with an asterisk (*). χ^2 = 0.79, R_{wp} = 3.59. (c) At 280(2) K the magnetic peaks have grown and are changing their relative intensity. χ^2 = 0.75, R_{wp} = 4.07. (d) At 1.5 K the magnetic peaks reflect the low temperature ordering regime. χ^2 = 0.85, R_{wp} = 4.05. Note the difference in the ratios of magnetic peaks between (b) and (d) resulting from the spin-reorientation. In the plots the data (blue), fit (red) and difference (gray) are shown. Tickmarks are from top $Sr_2CrO_2Cr_2As_2$ nuclear (94.6 % by mass), $Sr_2CrO_2Cr_2As_2$ magnetic, CsI (1.2 %), CrAs (1.2 %), Cr_4As_3 (0.9 %), Cr_2As (1.0 %) and Sr_2CrO_3CrAs (1.3 %). Sr (green), As (orange) and O (red) atoms are also depicted.

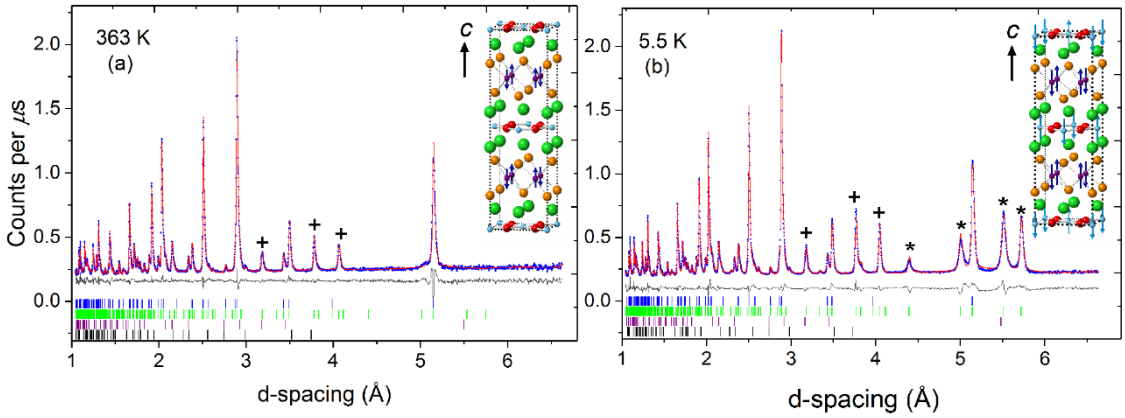

Figure 5. Rietveld refinement against PND data for $Ba_2CrO_2Cr_2As_2$ at (a) 363 K and (b) 5.5 K from WISH bank 3/8 (2θ = 90°). The insets depict the ordering and relative magnitudes of the magnetic moments. Data (blue), fit (red) and difference (gray) are shown. Tickmarks are from top $Ba_2CrO_2Cr_2As_2$ nuclear, $Ba_2CrO_2Cr_2As_2$ magnetic, Cr_2As (9.1% by mass) and $BaCr_2As_2$ (0.7%). + indicates magnetic Bragg peaks arising from ordering of the Cr(2) moments (dark blue) and * indicates magnetic Bragg peaks arising from ordering of the Cr(1)moments (light blue). Ba (green), As (orange) and O (red) atoms are also depicted.

For $Sr_2CrO_2Cr_2As_2$ additional magnetic reflections (those labelled with (*) in Figure 3(a) and Figure 4) became apparent, and these emerge between 325 K and 348 K and persist to lower temperatures. Similar reflections emerge in $Ba_2CrO_2Cr_2As_2$ below 233 K (Figure 3(b) and Figure 5). New magnetic models were deduced for both compounds in which the moments of the Cr(1) ions in the oxide layer participate in long range order with

antiferromagnetic coupling of nearest neighbour moments. For these moments the propagation vector is k = (½ ½ 0) (requiring a $\sqrt{2}a_{nucl} \times \sqrt{2}a_{nucl} \times c_{nucl}$ magnetic unit cell). However the details of these magnetic models are different in $Sr_2CrO_2Cr_2As_2$ and $Ba_2CrO_2Cr_2As_2$, and in particular the magnetic scattering of $Sr_2CrO_2Cr_2As_2$ shows some anomalies as described below which have not been observed previously.[13] In $Ba_2CrO_2Cr_2As_2$ the fits to the data below 233 K (Figure 5(b)) are consistent with Cr(1) oxide layer moments that are directed, like the Cr(2) arsenide layer moments, parallel to the *c* direction. On cooling, the Cr(1) long range ordered moment grows in magnitude and becomes larger than the Cr(2) long range ordered moment below 200 K. At the lowest temperature both moments in $Ba_2CrO_2Cr_2As_2$ are saturated and are directed parallel to the *c* axis.

In contrast, just below 348 K in $Sr_2CrO_2Cr_2As_2$ the major component of the Cr(1) moment lies in the *ab*-plane parallel to the CrO_2 layers, with an antiferromagnetic nearest neighbour Cr(1) coupling arrangement similar to that found for the Mn moments in the MnO_2 layers of $Sr_2MnO_2Mn_2Sb_2$,[3] but orthogonal to that found at the onset of ordering of these Cr(1) moments in $Ba_2CrO_2Cr_2As_2$. In $Sr_2CrO_2Cr_2As_2$ the magnetic intensities were satisfactorily modelled when these moments were slightly canted towards the *c*-axis direction as shown in Figure 4(b) for the data collected at 297(1) K. Refinement of a canting of the Cr(2) moments towards the *ab*-plane was also attempted. At 297 K the refined value of the canted component did not deviate from zero and at 290 K the value was 0.2(2) μ_B.

In $Sr_2CrO_2Cr_2As_2$ the magnitude of the Cr(1) (oxide layer) ordered moment at 297 K is 1.61(1) μ_B. This increases rapidly on cooling and overtakes the magnitude of the Cr(2) (arsenide layer) moments by 248 K. Between these temperatures, a gradual reorientation

of the direction of both sets of moments takes place in $Sr_2CrO_2Cr_2As_2$: the Cr(1) moments in the oxide layer rotate from the *ab*-plane to lie along the *c*-axis, and the Cr(2) moments in the arsenide layer rotate *vice versa*. This behaviour of $Sr_2CrO_2Cr_2As_2$ has recently been reported by Liu *et al.*[13] and our results are consistent with theirs. We note here that our PND measurements in this reorientation region straddling room temperature were measured on warming in the cryostat which was not optimised for controlling temperature or measuring the sample temperature in this range. It was evident from the comparison of the magnetic scattering intensities of sample 1 inside the cryostat with the magnetic scattering intensities measured for both samples 1 and 2 at room temperature outside the cryostat, that the sample temperature was systematically overestimated by the cryostat thermocouple. So calibration of the sample temperature was performed using the behaviour of the lattice parameters of both the main phase and CsI impurity, and these are the temperatures quoted in the text (See Figure S1 and Table S7).

The spin re-orientation is, as suggested by Liu *et al.*,[13] presumably the origin of the feature in the magnetic susceptibility and the heat capacity noted by Jiang *et al.*[12] Refinement of the magnetic structure at 280(2) K (Figure 4(c)), shows the majority component of the Cr(1) moments in the oxide layer is now directed along the *c*-axis and the Cr(2) spins in the arsenide layer are now significantly rotated onto the *ab*-plane, with a larger component of the moment lying in the *ab* plane than in the *c*-direction. The moments on the Cr(1) and Cr(2) sublattices remain orthogonal.

By 247(1) K attempted refinement of a remanent *ab*-component in the Cr(1) moment for $Sr_2CrO_2Cr_2As_2$ produced a value of 0.73(2) μ_B and refinement of a remanent *c*-component for the Cr(2) moment produced a value of 0.77(3) μ_B although the agreement factors were only marginally smaller (>0.05%) than when these minority components

were set to zero. So, within the certainty of the measurement, the spin-reorientation transition (SRT) appears to be complete. So at this temperature and below in $Sr_2CrO_2Cr_2As_2$, the Cr(2) moments in the arsenide layer are, within the experimental uncertainty, directed completely within the *ab*-plane and the Cr(1) moments in the oxide layer are directed purely along the *c*-direction. This arrangement of the moments is observed to persist at all lower temperatures, with the moments on both Cr(1) and Cr(2) sublattices reaching saturation at around 100 K. The refinement at 1.5 K is shown in Figure 4(d). Note that powder neutron diffraction measurements place an intrinsic constraint on knowing the moment orientation in an ordered system.[35] The component along the principal *c* axis may be determined unambiguously, but the orientation of any component within the (*ab*) plane perpendicular to the principal axis is uncertain.

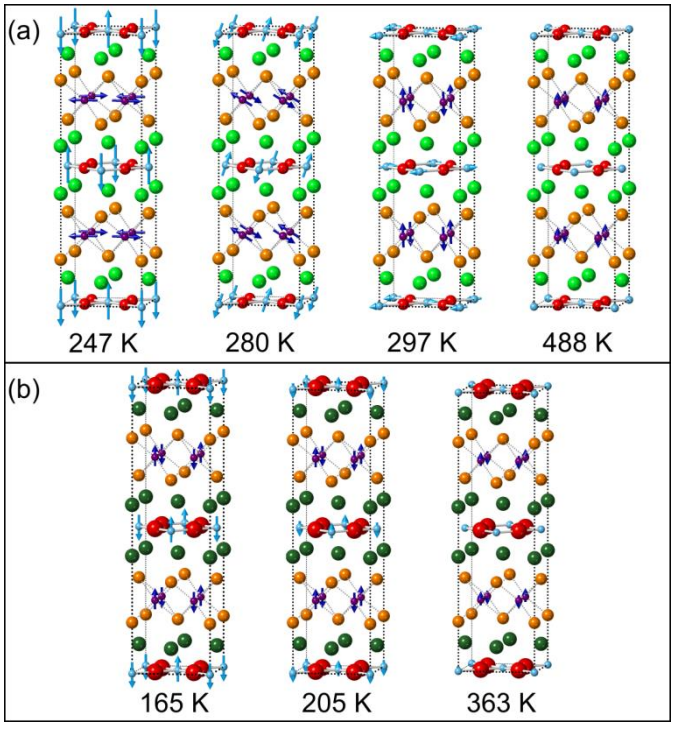

Figure 6. (a) Magnetic unit cell of $Sr_2CrO_2Cr_2As_2$ over the temperature range 1.5 – 623 K, showing the magnitude and direction of magnetic moments for the two chromium sublattices. (b) analogous diagrams showing the evolution in $Ba_2CrO_2Cr_2As_2$

Figure 6(a) summarises the changes in the magnetic model for $Sr_2CrO_2Cr_2As_2$ with temperature and Figure 7(a) and 7(b) show the changes in the magnitudes of the refined moments and their components. In contrast $Ba_2CrO_2Cr_2As_2$ shows no spin-reorientation transition and both Cr(2) and Cr(1) moments are oriented along the *c* direction (Figure 6(b) and 7(c)).

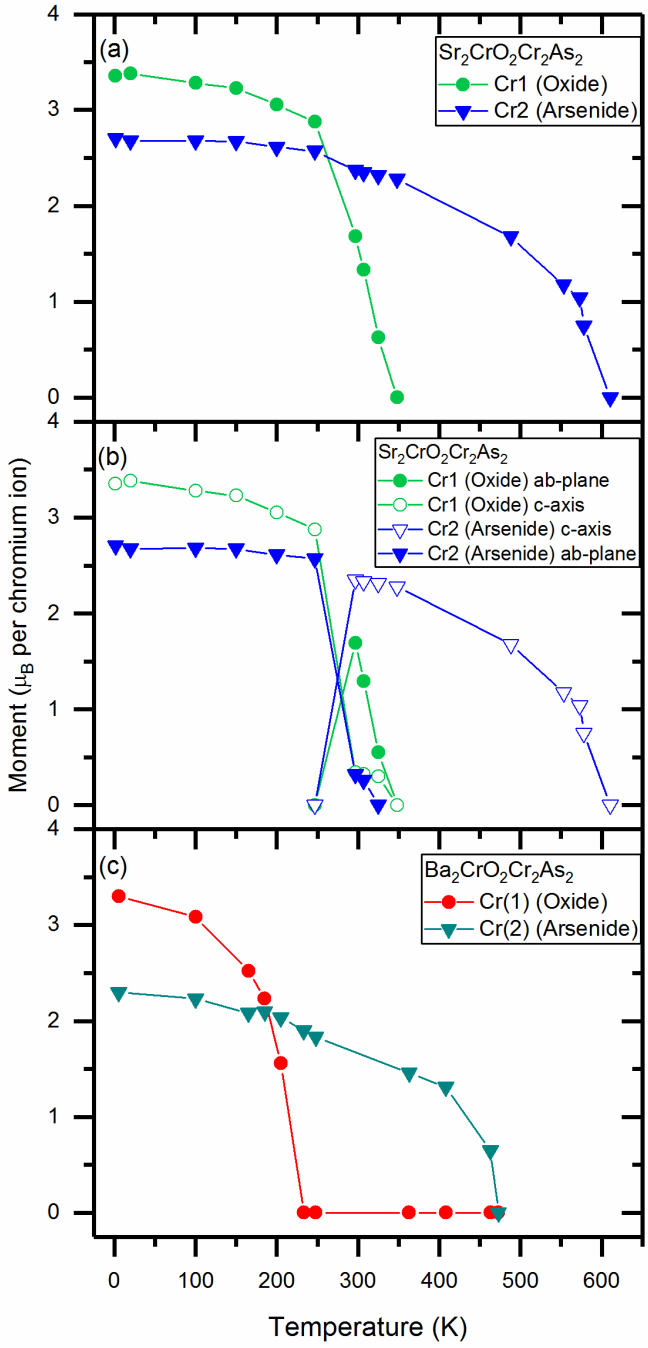

Figure 7. (a) Magnitudes and (b) magnitudes and directions of the long range ordered moments in the two Cr sublattices of $Sr_2CrO_2Cr_2As_2$ as functions of temperature. (c) Magnitudes of the moments in the two Cr sublattices of $Ba_2CrO_2Cr_2As_2$ as a function of temperature.

The high resolution across a wide *d*-spacing range available on the WISH instrument enabled us to observe clearly two further features of the magnetic scattering in $Sr_2CrO_2Cr_2As_2$ that were not present in $Ba_2CrO_2Cr_2As_2$ and which may be important in explaining why the spin-reorientation transition found by us and by Liu *et al.*[13] occurs in $Sr_2CrO_2Cr_2As_2$ given that two sublattices ordering with different propagation vectors should not, in principle, couple to one another. These features have not been described previously. Firstly, we observed in the low-angle data bank on WISH the emergence between 280(2) K and 247 K of a further feature in the long *d*-spacing region at about 16.2 Å. This feature, which we presume to be magnetic in origin, because there is no corresponding feature in 100 K X-ray diffraction data (Figure S12), is at a similar *d*-spacing to the intense 0 0 1 reflection of a minor impurity identified as Sr_2CrO_3CrAs with the Sr_2MnO_3CuS structure.[36] However on further cooling it moves significantly to longer *d*-spacings (it moves much more, and in the opposite direction to that expected for thermal contraction) as shown in Figure 8, reaching 16.8 Å at 1.5 K.

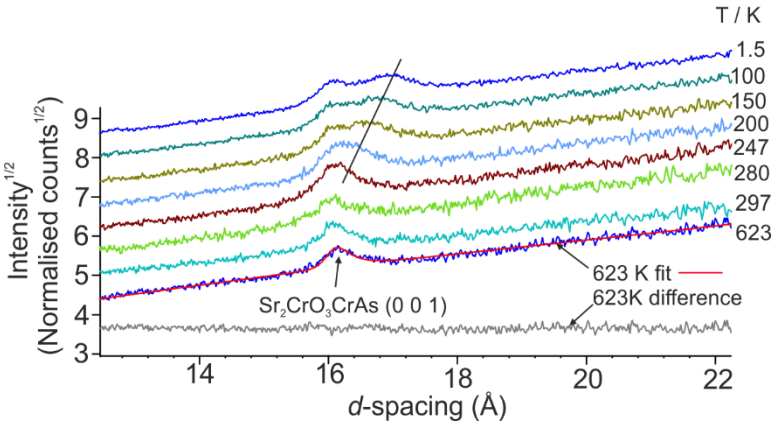

Figure 8. The extra magnetic scattering at long *d*-spacings visible in the low angle ($2\theta = 27°$) data banks on WISH. The intense (0 0 1) nuclear reflection of the Sr_2CrO_3CrAs impurity (1.3 % by mass) is fitted against the 623 K data. The extra scattering emerges from a similar *d*-spacing at the temperature of the spin reorientation transition in the main $Sr_2CrO_2Cr_2As_2$ phase and shifts markedly to longer *d*-spacings on further cooling as shown by the guideline. The patterns are offset by 0.6 units along the intensity$^{1/2}$ axis. See Figure S12 for comparative X-ray data showing the lack of this additional scattering.

Secondly, below 290 K in $Sr_2CrO_2Cr_2As_2$ a slight discrepancy occurs between the locations of the magnetic peaks and the positions predicted on the basis of the tetragonal structural unit cell. The discrepancy is only clearly evident in the fit to the (101/011) and (010/100) reflections for the magnetic unit cell, which lie at *d*-spacings of 5.42 and 5.66 Å, respectively. These are purely magnetic reflections (they correspond to the (½ ½ 1) and (½ ½ 0) reflections for the nuclear unit cell). From 280 K down to 1.5 K, the discrepancy can be well accounted for by refining the *a* and *b* lattice parameters of the magnetic unit cell independently of one another with the *c* lattice parameter fixed to that of the nuclear unit cell. Model independent (Pawley) fits to the 1.5 K data from WISH banks 3/8 & 5/6 improved from a R_{wp} of 4.24 % when the structural and magnetic cells were constrained to be tetragonal with $a_{mag} = \sqrt{2} \times a_{nucl.}$ to R_{wp} = 2.89 when the nuclear cell was constrained to be tetragonal and the magnetic cell was allowed to be orthorhombic. A further slight decrease in R_{wp} to 2.62 % was found when the nuclear cell was also allowed to be orthorhombic, thus suggesting a possible small orthorhombic distortion occurring in the structure below 290 K. Figure 9 shows the effect on the long *d*-spacing magnetic reflections of fitting the pattern using a single Pawley (model independent) phase which was either tetragonal (Figure 9(a)) or orthorhombic (Figure 9(b)). Applying this method of modelling to the 100, 150, 200, 250, and 280 K data shows a decrease in the degree of the apparent orthorhombic distortion on warming, accompanied by a convergence of the agreement factors when modelling the magnetic peaks as either tetragonal or orthorhombic (Figure S2 and Table S8). The apparent distortion of the unit cell follows the growth in the magnitude of the component of the Cr(2) moments in the arsenide layer directed in the *ab* plane (Figure 7(b)) suggesting that

it is associated with the spin reorientation. We examined this behaviour further by running WISH in "double-frame" mode in which alternate neutron pulses were discarded, allowing the relevant range of *d*-spacings to be probed on a higher resolution detector bank. The behaviour was observed to be similar and we rule out that it is an artefact of the measurement.

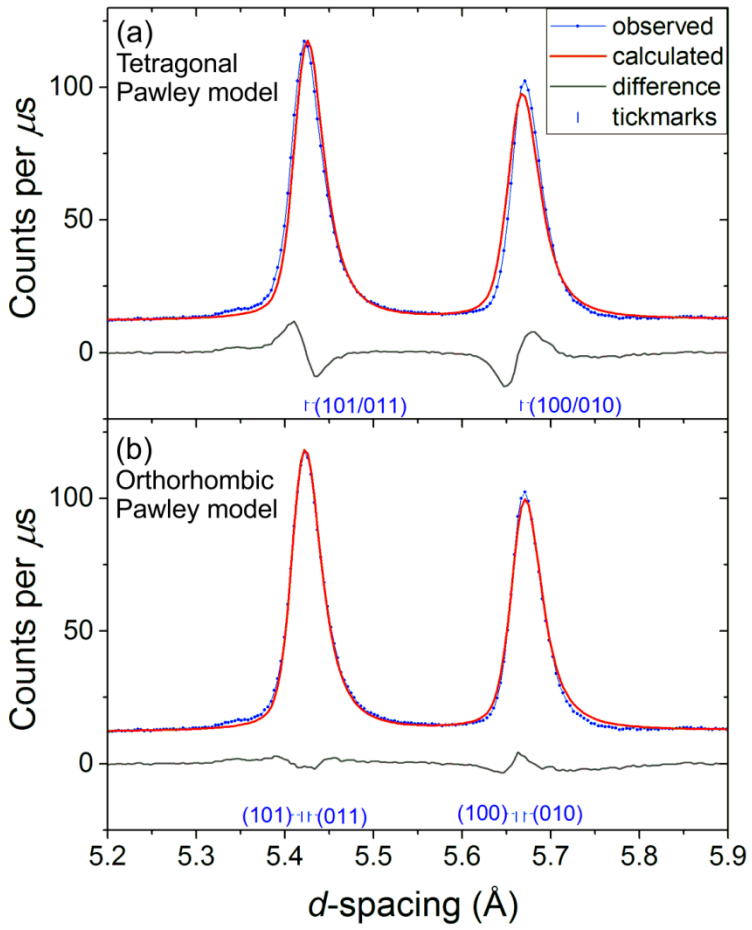

Figure 9. Comparison of the fit when using (a) a tetragonal or (b) an orthorhombic model and refining the unit cell metric and peak intensities independently of the structure (Pawley refinement). Fitting was carried out against all 5 detector banks, including the Pawley refinement of the magnetic peaks only and Rietveld refinement of the nuclear peaks of tetragonal $Sr_2CrO_2Cr_2As_2$ (95.3%), CsI (1.2%), CrAs (1.2%), Cr_4As_3 (1.3%) and Cr_2As (1.0%). The agreement factor R_{wp} for the fit as a whole drops from 4.27 % with the tetragonal model to 3.54 % with the orthorhombic model. The indices for these purely magnetic reflections refer to the $\sqrt{2}a \times \sqrt{2}a \times c$ expansion of the nuclear cell.

We probed whether there really was a symmetry lowering of the crystal structure via exchange-striction by performing measurements of the X-ray diffraction pattern with a higher reciprocal space resolution using the synchrotron powder diffractometer I11 at Diamond and measuring data using the high resolution MAC detector. This showed no evidence of the nuclear unit cell undergoing any distortion between ambient temperature and 100 K (Figure S4), although the reciprocal space resolution is about five times higher on I11 ($\Delta d/d$(FWMH) ~ 2×10^{-3} at d ~ 2 Å) than on WISH (($\Delta d/d$(FWMH) ~ 10^{-2}). Furthermore no sharp transitions are evident in the behaviour of the lattice parameters or unit cell volume in the range 100 K to 673 K and the behaviour is qualitatively similar to that shown by the CsI impurity (Figure S5). Low temperature electron diffraction measurements (Figure S8) also offered no evidence for a structural change. Thus, the slight shift of the purely magnetic peaks in Figure 9(a) from their expected positions is not simply a consequence of a structural distortion.

Discussion and Conclusions.

Crystal structures. The structure type accommodates a range of cations and anions. In comparing $Sr_2CrO_2Cr_2As_2$ with the Ba analogue, significant changes in the interatomic distances (Table 1) result from the increase in size of the alkaline earth cation. The *a* lattice parameter and hence the Cr(1)–O and Cr(2)–Cr(2) distances increase by 1.17 % on substituting Sr^{2+} for Ba^{2+}. The Cr(2)–As distance in the arsenide layers increases only marginally (0.3 %) so the $Cr(2)As_4$ tetrahedra which are slightly compressed in the *ab* plane become more regular in $Ba_2CrO_2Cr_2As_2$. With the basal plane expansion restricted by maintaining strong Cr(1)–O and Cr(2)–As interactions, the larger Ba^{2+} cation is

accommodated disproportionately by expansion of the cell perpendicular to the basal plane and the *c* lattice parameter increases by 9.3%. Thus the most significant change in coordination environment for a Cr ion is the 14 % increase in the Cr(1)–As distance, from 3.207(1) Å in $Sr_2CrO_2Cr_2As_2$ to 3.663(1) Å in $Ba_2CrO_2Cr_2As_2$ which makes the already highly distended $Cr(1)O_4As_2$ environment even more distended and in $Ba_2CrO_2Cr_2As_2$, Cr(1) is close to being in a purely square planar CrO_4 coordination environment.

Since Cr^{2+} with the high spin d^4 configuration is strongly Jahn-Teller active when in an octahedral coordination environment, it is worth making comparison with the crystal structures of other known Sr-containing members of this structural series (Table 5). On comparison with the analogous manganese, iron and zinc compounds in the series, trends are observed in the size of the lattice parameters which can be explained in terms of the differing ionic radii of the metals.

Table 5. Lattice parameters and selected bond distances for reported $Sr_2Mn_3As_2O_2$-type oxide arsenides with different 1st row transition metals or Zn.

Compound	$Sr_2CrO_2Cr_2As_2$	$Sr_2CrO_2Fe_2As_2$	$Sr_2MnO_2Zn_2As_2$	$Sr_2MnO_2Mn_2As_2$
Reference	This work	26	11	3
T (K)	298	298	298	300
a (Å)	4.00806(3)	3.9948(1)	4.12624(3)	4.1500(4)
c (Å)	18.8216(2)	18.447(1)	18.6709(2)	18.867(2)
c/*a*	4.6959(1)	4.6178(3)	4.5249(1)	4.546(1)
M(1)–As (Å)	3.2063(6)	3.234(2)	3.12680(3)	3.189(7)
M(1)–O (Å) = *a* / 2	2.00403(1)	1.99740(5)	2.06149(1)	2.075(1)
M(1) Bond Distance Ratio[a]	1.5999(3)	1.619(1)	1.51677(2)	1.537(3)
M(2)–As (Å)	2.5073	2.426(1)	2.57192(1)	2.577
M(2)–M(2) (Å) = *a* /√2	2.834	2.825	2.918	2.934
As–*M*(2)–As (deg) [2]	106.40	110.80(2)	106.56(3)	107.254

[a]The *M*(1) bond distance ratio given is the *M*(1)–As distance divided by the *M*(1)–O distance.

The most significant comparison is to be made between $Sr_2CrO_2Cr_2As_2$ and the analogous Mn-containing compound $Sr_2MnO_2Mn_2As_2$. Both lattice parameters are significantly shorter in the case of the Cr compound in line with the smaller ionic radius of the d^4 Cr^{2+} ion (0.80 Å)[37] compared with the d^5 Mn^{2+} ion (0.83 Å) with an additional antibonding *d* electron. The Cr(2)–Cr(2) distance (equal to $a / \sqrt{2}$) across the shared edges of adjacent $CrAs_4$ tetrahedra is 3.4 % shorter than the corresponding distance in $Sr_2MnO_2Mn_2As_2$ and the Cr(2)–As distances in the $CrAs_4$ tetrahedra of 2.5073 Å are 2.7 % shorter than the corresponding Mn(2)–As distances in $Sr_2MnO_2Mn_2As_2$, although the distortion of the $CrAs_4$ tetrahedron from regular (slight compression along the tetragonal axis) is only marginally larger than in the Mn case. In the oxide layers the transition metal ion is forced, by the presence of the intervening Sr^{2+} cation, to occupy a highly distended octahedral environment MO_4As_2 with *M*(1)–As distances that are much larger than in the MAs_4 tetrahedra, reflecting a rather weak interaction between *M*(1) and As. In $Sr_2CrO_2Cr_2As_2$ the Cr(1)–O distance (equal to *a* / 2) is 3.4 % shorter than the Mn(1)–O distance in $Sr_2MnO_2Mn_2As_2$ while the long Cr(1)–As distance is 0.5 % longer than the corresponding Mn(1)–As distance in $Sr_2MnO_2Mn_2As_2$. The result of accommodating a relatively small ion in the arsenide layer *and* satisfying the coordination requirements of the Sr^{2+} ions results in a CrO_4As_2 coordination environment that is a rather more distended octahedron than that of the corresponding MnO_4As_2 environment. Although d^4 ions such as Cr^{2+} adopt strongly Jahn-Teller distorted octahedral environments in molecules and solids, the ratio of the Cr(1)–As and Cr(1)–O distances of 1.6 in $Sr_2CrO_2Cr_2As_2$ is even larger than the measured Cr–Cl: Cr–O ratio of 1.33 in $Cr(H_2O)_4Cl_2$ [38] which is elongated along the Cr–Cl bonds (note that, for comparison, Sr–As ~ 3.1 Å[39] and Sr–Cl ~3.02 Å[40] distances are fairly similar, so, for the purposes of comparison, we use Cr–Cl distances as a proxy for Cr–As distances), and larger than one

would expect based on the ratio of axial and equatorial Cr–Cl distances (4 × 2.39 Å and 2 × 2.90 Å) in the crystal structure of $CrCl_2$.[41] So it is not clear that the increased axial distention around the Cr(1) site in $Sr_2CrO_2Cr_2As_2$ compared with the case in $Sr_2MnO_2Mn_2As_2$ is driven by a Jahn-Teller stabilisation. In these compounds it is probably best to consider the distended $M(1)O_4As_2$ environment as being a consequence of the crystal structure, and this is clear when Sr^{2+} is substituted by Ba^{2+} as the distention becomes very much larger in $Ba_2CrO_2Cr_2As_2$ than could be attributed to a Jahn-Teller distortion (Table 1, Figure 1).

Magnetic Ordering. The observation that the Cr(2) moments in the Cr_2As_2 layer order at a much higher temperature than the Cr(1) moments in the oxide layer is consistent with the observations of Brock *et al.* for the Mn analogues $Sr_2MnO_2Mn_2As_2$ and $Sr_2MnO_2Mn_2Sb_2$.[3,4] However while the ordering temperature for the Mn(2) moments in the Mn_2As_2 layer is 340 K in $Sr_2MnO_2Mn_2As_2$, the corresponding Néel temperature (T_{N1}) in the chromium case $Sr_2CrO_2Cr_2As_2$ is 600(10) K. Similarly, the Cr(1) magnetic sublattice of the CrO_2 layers of $Sr_2CrO_2Cr_2As_2$ has a Néel temperature (T_{N2}) estimated as 330(5) K from the PND measurements, whereas in $Sr_2MnO_2Mn_2As_2$ only short range ordering of the Mn(1) moments in the MnO_2 layer is observed, and not until temperatures below 75 K. The considerably higher ordering temperatures in the chromium case are consistent with the observed bond distances. Shorter Cr(2)–Cr(2) and Cr(1)–O distances within the layers, compared with those in the Mn analogue, combined with the less-contracted 3*d* orbitals of Cr should facilitate stronger intraplanar exchange interactions (via direct Cr(2)–Cr(2) exchange interactions, and Cr(2)–As–Cr(2) and Cr(1)–O–Cr(1) superexchange). Indeed, the manganese oxyantimonide of the series, $Sr_2MnO_2Mn_2Sb_2$ with a larger *a* lattice parameter, has an ordering temperature of the Mn^{2+} ions in the

pnictide layer of 300 K, lower than that of the oxyarsenide (340 K). Accordingly, the longer Cr(2)–Cr(2) and Cr(1)–O distances in $Ba_2CrO_2Cr_2As_2$ result in both Cr sublattices undergoing magnetic long range order at significantly lower temperatures than in $Sr_2CrO_2Cr_2As_2$ (Figure 7).

The other clear differences between $Sr_2CrO_2Cr_2As_2$ and $Ba_2CrO_2Cr_2As_2$ and between these Cr compounds and the Mn analogues lie in the orientations of the moments, and in the re-orientation transition that is evident in $Sr_2CrO_2Cr_2As_2$ from our work and that of Liu *et al.*[13] Firstly we consider the factors that favour particular orientations of moments relative to the crystal axes. The orientation of the magnetic moments of ions in a magnetically ordered array relative to the ligand field may be rationalised on the basis of considerations of spin-orbit coupling as described by Whangbo *et al.*[42] Because the ligand field does not entirely quench the orbital angular momentum for a 3*d* transition metal ion, the *d* orbitals remain associated with their L_z values from the free ion case, if the difference $|\Delta L_z|$ in L_z values between the highest occupied orbital and the lowest unoccupied orbital is 0 then the prediction is that the magnetic moment lies along the *z* direction where *z* is the principal axis. If $|\Delta L_z| = 1$ then the moment is predicted to lie perpendicular to the *z* direction – i.e. in the *xy* plane. In the case of $Sr_2CrO_2Cr_2As_2$ and $Ba_2CrO_2Cr_2As_2$ the Cr(1) moments in the oxide layer have highly axially distended octahedral ligand fields (Figure 1) resulting in an orbital arrangement similar to that shown in Figure 10. This leads to the prediction that the moment will lie along the *z* direction (i.e. the crystallographic *c* axis) according to the argument in Figure 6(a) of ref 42. This is exactly in accord with what we find for the Cr(1) oxide layer moments in $Ba_2CrO_2Cr_2As_2$ from the onset of their ordering at 233 K and for $Sr_2CrO_2Cr_2As_2$ below 247 K after the spin-reorientation transition is complete. Other experimental cases bear

this out. For example the n = 1 Ruddlesden-Popper-type phase $LaSrMnO_4$[43] contains Mn^{3+} ions with the $3d^4$ configuration are in Jahn-Teller-distorted MnO_6 octahedra that have their two longer Mn–O bonds directed along the principal axis of the tetragonal crystal. In this case, which is isoelectronic with the case of $Sr_2CrO_2Cr_2As_2$ and $Ba_2CrO_2Cr_2As_2$, the moments are also found experimentally to lie parallel to the principal axis, in line with the predictions of ref 42.

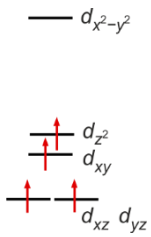

Figure 10. Schematic of the *d*-orbital splitting in the distended CrO_4As_2 ligand field.

The corresponding magnetic ions in the oxide layers of $Sr_2MnO_2Mn_2Pn_2$ are Mn^{2+} d^5 moments and their directional preference is weaker because formally the d^5 configuration carries no orbital angular momentum. Experimentally the Fe^{3+} d^5 moments in $LaSrFeO_4$,[44] $CaPrFeO_4$[45] and $CaNdFeO_4$[46] are observed to be aligned perpendicular to the crystallographic c axis at temperatures above the magnetic ordering temperature of the lanthanide moments, and in these cases the Fe^{3+} ions are in axially distended FeO_6 octahedra ($Fe–O_{ax}$ / $Fe–O_{eq}$ = 1.11 at room temperature), so the ligand fields are qualitatively similar, although less axially distended, to that in $Sr_2MnO_2Mn_2Sb_2$. Thus the Mn(1) ordered moments in the MnO_2 sheets in $Sr_2MnO_2Mn_2Sb_2$ are oriented in a similar way (within the *ab* plane) to analogous antiferromagnetic d^5 systems, and perpendicular to the direction which is predicted and found for d^4 Cr^{2+} and Mn^{3+} moments.

Experiments reveal that the Mn^{2+} (d^5) and Cr^{2+} (d^4) moments in LaMnAsO, LaCrAsO $BaMn_2As_2$ and $BaCr_2As_2$[30] all undergo antiferromagnetic ordering with their Mn or Cr moments aligned parallel to the *c* axis. This is also the experimentally-observed orientation of the moments corresponding to the Mn(2) (d^5) or Cr(2) (d^4) ions in $Sr_2MnO_2Mn_2Pn_2$ and $Ba_2CrO_2Cr_2As_2$ (at all temperatures) or $Sr_2CrO_2Cr_2As_2$ (at temperatures above the ordering temperature of the Cr(1) moments). So we conclude that these are the preferred moment orientations for these tetrahedral moments. Thus in $Ba_2CrO_2Cr_2As_2$ and $Sr_2MnO_2Mn_2Sb_2$ where there is long range magnetic order on both transition metal sublattices, the preferred moment directions on both sublattices are found experimentally below the respective ordering temperatures.

Like $Ba_2CrO_2Cr_2As_2$, but in contrast to the $Sr_2MnO_2Mn_2Pn_2$ cases, $Sr_2CrO_2Cr_2As_2$ contains two sublattices of Cr^{2+} moments which both have a preference, for alignment along the *c* axis. In all these compounds the two different transition metal moments order with different propagation vectors (k = (1 1 1) for the Cr(2) (or Mn(2)) moments in the pnictide layers and k = (½ ½ 0) for the Cr(1) (or Mn(1)) moments in the oxide layers. There should thus be no direct coupling between the Cr(1) and Cr(2) sublattices. However we (and Liu *et al.*[13]) observe that in $Sr_2CrO_2Cr_2As_2$ ordering of the Cr(1) moments in the oxide layer drives a spin-reorientation transition as the magnitude of the ordered Cr(1) moment increases (Figures 6(a) & 7(b)) with the moments on the two sublattices remaining orthogonal. Thus, the sublattices must communicate, and there is a preference for the moments to be orthogonal (see below). We propose that the preference for alignment parallel to *c* is stronger for the Cr(1) ions in the oxide layer than it is for the Cr(2) moments in the arsenide layer, presumably due to the greater anisotropy of the ligand field, and this presumably accounts for the magnetic ground state. The spin-

reorientation transition in $Sr_2CrO_2Cr_2As_2$ bears some qualitative resemblance to the spin-reorientations driven by the ordering of lanthanide moments in compounds containing Mn*Pn* layers (e.g. the CeMnAsO,[20,53] NdMnAsO[18,19] and PrMnSbO,[47] members of the *Ln*MnAsO series) and layered perovskite-related compounds containing ordered arrays of transition metal moments (e.g. $CaNdFeO_4$[46] and $CaPrFeO_4$[45]), but in these cases direct coupling of the transition metal and lanthanide magnetic sublattices is permitted because they order with the same propagation vector.

While powder neutron diffraction measurements place an intrinsic constraint on knowing the moment orientation in an ordered system,[35] we note that for the tetragonal system, the moment component along the principal *c* axis may be determined unambiguously, while the orientation of any component within the (*ab*) plane perpendicular to the principal axis is uncertain. In $Sr_2CrO_2Cr_2As_2$ with one moment parallel to *c*, and one moment perpendicular to *c* it is clear that the Cr(1) and Cr(2) moments are orthogonal. Thus exchange interactions that rely on scalar products of the spins of these two sublattices (e.g. Heisenberg symmetric exchange or biquadratic exchange) will be zero, while terms that are vector products of the spins (Dzyaloshinskii-Moriya (DM) antisymmetric exchange) will be non-zero. A DM interaction between the orthogonal Cr(1) and Cr(2) moments could, in principle, be responsible for maintaining their orthogonality. The strength of the DM interaction depends on the size of the spins, on the spin-orbit coupling constant of the Cr^{2+} ions and on the size of the unquenched orbital moment of the ions.[48] In this case the d^4 Cr(2) ion in a slightly distorted tetrahedral environment is expected to carry a significant orbital moment, and would result in a significant DM interaction.

For the DM interaction to provide this orthogonality however requires the two sublattices to couple. The group theoretical analysis presented in the Supporting Information (Figure

S6 and Figure S7 plus accompanying description) describes a likely structural distortion with tilting of the CrO_2 sheets and in-plane antipolar displacements of the Sr and As atoms. However, high resolution diffraction data from I11 at temperatures below and across the spin-reorientation transition gave no evidence for such a distortion: the refinements were not unstable, but there was no clear improvement to the fit and the displacements of atoms from their ideal positions (i.e. those of the *I*4/*mmm* structure) were a factor of 10 – 100 smaller than the uncertainties in the refined parameters.

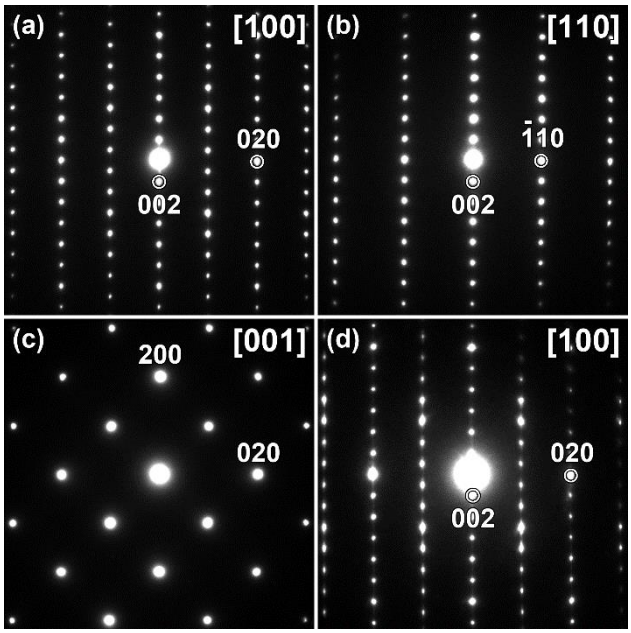

Figure 11. Representative ED patterns taken along the main directions: [100] (a), [110] (b) and [001] (c). The majority of crystals probed produced diffraction patterns as in (a)-(c), corresponding to the well ordered structure for which the HAADF-STEM image is shown along [100] in Figure 12(a). The [100] ED pattern in (d) shows the presence of diffuse streaks along 0k0 lines as a consequence of the stacking faults found in some of the crystallites (Figure 12(b)).

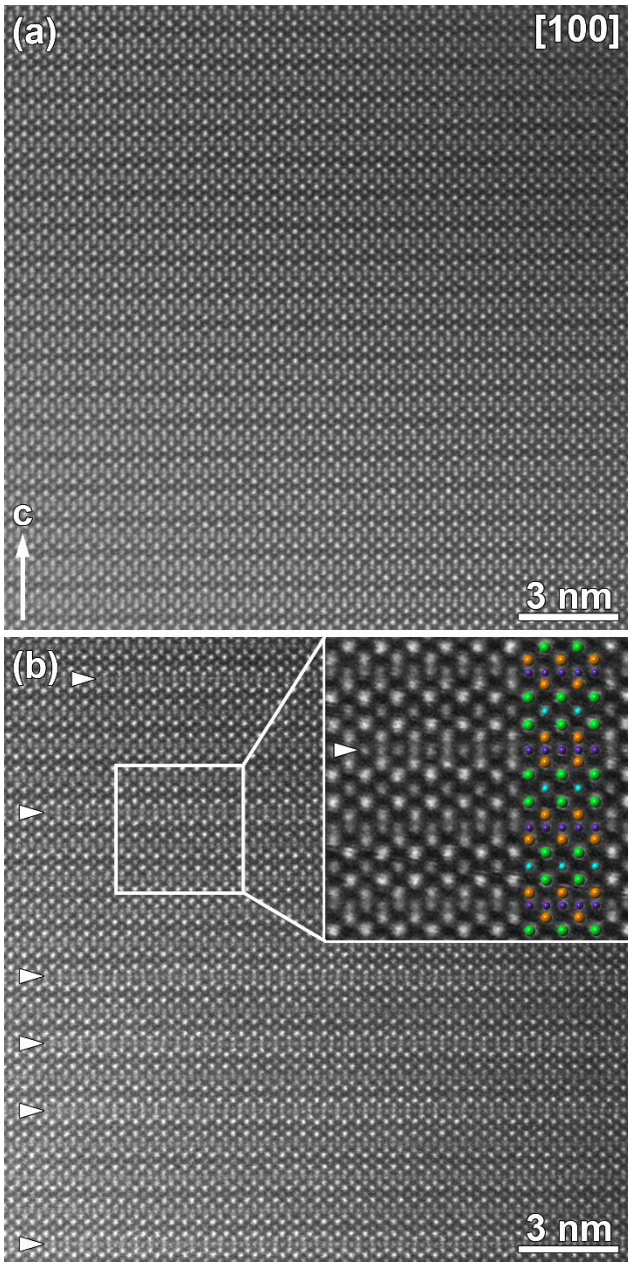

Figure 12. HAADF-STEM images taken from a well-ordered crystal (a) and a crystal with stacking faults (b). The atom identities are inserted on the enlarged image in (b) (Sr – green; As – orange; Cr1 – turquoise; Cr2 – violet; oxygen atoms are not shown for clarity). The randomly distributed stacking faults are indicated with arrowheads See also Figure S9 and Figure S10.

We probed $Sr_2CrO_2Cr_2As_2$ further using electron microscopy. Room temperature electron diffraction (ED) patterns taken along the main crystallographic directions on different crystallites agree with the *I*4/*mmm* space group (Figure 11(a) - (c)). No additional extinction conditions were evident in these patterns that suggested a symmetry lowering, nor were any changes evident on cooling to ~100 K (~-170 °C), well below the spin-reorientation transition. HAADF-STEM experiments did reveal further structural features of $Sr_2CrO_2Cr_2As_2$ which were not evident from the bulk diffraction measurements. The HAADF-STEM images in Figure 12(a) show well-ordered regions, consistent with the sharp ED patterns in Figure 11(a)-(c), however diffuse streaks were observed on some ED patterns acquired along the [100] direction (Figure 11(d)) suggesting large concentrations of stacking faults. The faults are characterised by the relative translation (by *a*/2) of the two planes of arsenide ions that form the CrAs layers (close-up in the HAADF-STEM image of a faulted region in Figure 12(b)). Figure 12(b) shows that these stacking faults can occur in quite high concentrations and a random manner. Occasionally, the stacking faults show long range order, resulting in additional reflections in the ED patterns (Figure S10). It is possible that these faults arise from slight oxidation of part of the sample with the conversion of a Cr_2As_2 layer to a Cr_2OAs_2 layer containing Cr_2O sheets similar to those found for other transition metals, notably Fe, in numerous compounds: $La_2Fe_2Se_2O_3$[49] and relatives such as $Sr_2Fe_2Se_2OF_2$,[50] $Na_2Fe_2Se_2O$,[51] and $BaFe_2Se_2O$,[52] This oxidation to produce Cr^{3+} ions in these layers is consistent with the facile oxidation of Cr^{2+}. However further investigation is required on this point. The electron microscopy measurements also identified a well-crystallised minority phase which was more oxide rich, and has the formula Sr_2CrO_3CrAs, isostructural with Sr_2MnO_3CuS,[36] with thicker oxide layers separating the CrAs layers. Adding this phase to the Rietveld refinements at the 1.3(1) % level by mass accounted

for weak reflections that could not be accounted for by other impurities (see Figure1, Figure 8). We have subsequently been able to synthesise this phase in the bulk form and its characterisation will be reported elsewhere.

Neither the electron microscopy measurements nor the high resolution synchrotron X-ray diffraction measurements provide evidence for a symmetry-lowering distortion that would allow the two magnetic sublattices to couple and enable the DM interaction to stabilise the orthogonal moments. Nevertheless the experimental observation by us and by Liu *et al.*[13] for $Sr_2CrO_2Cr_2As_2$ is that the ordering of the Cr(1) moments precipitates a spin reorientation of the already-ordered Cr(2) moments and the Cr(1) and Cr(2) moments maintain orthogonality, and this must be enabled by some other mechanism.

In CeMnAsO[20] where there is also a spin-reorientation transition, the behaviour of the magnetic reflections suggested an orthorhombic distortion at low temperature in data collected using a fairly high resolution neutron powder neutron diffractometer (OSIRIS at ISIS[20]), but in that case we went on to show that no symmetry-lowering distortion was observed in the low temperature powder X-ray diffraction, collected at much higher resolution using the synchrotron beamline ID31 at ESRF, although there was a decrease in the *c/a* ratio at the spin-reorientation transition in CeMnAsO (also noted by Zhang *et al.*[53]). We proposed that a very small incommensurability of the magnetic and nuclear structures could account for the behaviour of CeMnAsO.[20] The behaviour at the spin reorientation transition in $Sr_2CrO_2Cr_2As_2$ seems similar to that in CeMnAsO, so a possible conclusion that would account for the spin reorientation is that the long range magnetic ordering has a small incommensurability with the underlying crystal structure and our assumption that the Cr(2) moments order with a propagation vector k = (1 1 1) and the Cr(1) moments order with propagation vector k = (½ ½ 0) is an oversimplification.

The experimental support for this incommensurability is the observation of shifts in magnetic Bragg peaks (see Figure 9) suggestive of a symmetry-lowering distortion, despite the lack of an evidence for this in the crystal structure, and by the appearance of the additional scattering observed at about d = 16.5 Å in the neutron diffractogram (Figure 8). Attempts to model the behaviour of the magnetic scattering using a more sophisticated model were not successful – the small relative shifts of the positions of the magnetic peaks in Figure 9 suggests that the incommensurate solution is a spin density wave with a propagation vector of (0.4995 0.5003 0), but attempted refinements set this back to the commensurate value of (½ ½ 0). $Ba_2CrO_2Cr_2As_2$, where there is no spin-reorientation transition, shows no evidence that its magnetic structure is incommensurate. The reason why $Ba_2CrO_2Cr_2As_2$ differs from the Sr analogue is unclear. The only significant structural difference between them is the much larger Cr(1)-As distance in $Ba_2CrO_2Cr_2As_2$,meaning that the $Cr(1)O_4As_2$ octahedron is much more distended in $Ba_2CrO_2Cr_2As_2$ compared with $Sr_2CrO_2Cr_2As_2$. It is not clear how this relates to the anomalous behaviour of $Sr_2CrO_2Cr_2As_2$, although it would presumably be a key factor in determining the strength of Cr(1) – Cr(2) coupling. We suggest that further insight into the spin-reorientation transition of $Sr_2CrO_2Cr_2As_2$ may be obtained in a single crystal neutron diffraction investigation supported by high level computation. Whether the faulting observed in some grains of the sample in the electron diffraction and STEM images is relevant to the magnetic behaviour, or is unrelated to it also requires further investigation, but at least underlines the structural complexity of these intergrowth phases. We note that $Sr_2Mn_{2.23}Cr_{0.77}As_2O_2$ a member of the solid solution between all-Mn and all-Cr end members has recently been reported and this also shows a complex series of magnetic transitions and spin reorientations.[54]

Acknowledgements.

We thank: the UK EPSRC (EP/M020517/1 and EP/P018874/1) and the Leverhulme Trust (RPG-2014-221) for funding; the ISIS pulsed neutron and muon source (RB1610357 and RB1700075) and the Diamond Light Source Ltd (EE13284 and EE18786) for the award of beam time. We thank Dr A. Baker and Dr C. Murray for support on I11.

Competing Interests.

The authors declare no competing interests.

Author Information.

X. X. and M. A. J. synthesised the samples and with S. J. Cassidy collected and analysed the diffraction and magnetometry data. M. B. and J. H. collected and analysed the electron diffraction and microscopy data. F. O. and P. M. provided technical support on WISH and analyzed the spin-reorientation. S. J. Clarke wrote the paper with input from the other authors.

Supporting Information

The Supporting Information file is available free of charge at https://pubs.acs.org/doi/10.1021/acs.inorgchem.XXXXXX.

Tables of refined parameters, analysis of variable temperature diffraction data, further Rietveld refinement results, magnetic symmetry analysis of the spin reorientation, further electron microscopy results, magnetometry data. (PDF)

References

(1) Brechtel, E.; Cordier, G.; Schäfer, H. Über Oxidpnictide: Zur Kenntnis von $A_2Mn_3B_2O_2$ mit A = Sr, Ba und B = As, Sb, Bi / On Oxidpnictides: Preparation and Crystal Structure of $A_2Mn_3B_2O_2$ with A = Sr, Ba and B = As, Sb, Bi, *Zeitschrift für Naturforsch. B A J. Chem. Sci.*, **1979**, *34*, 777–780.

(2) Stetson, N. T.; Kauzlarich, S. M. A new material with alternating metal-oxide and metal-phosphide layers: barium manganese phosphate ($Ba_2Mn_3P_2O_2$), *Inorg. Chem.* **1991**, *30*, 3969-3971.

(3) S. L. Brock, N. . Raju, J. . Greedan and S. M. Kauzlarich, The magnetic structures of the mixed layer pnictide oxide compounds $Sr_2Mn_3Pn_2O_2$ (Pn = As, Sb), *J. Alloys Compd.*, **1996**, *237*, 9–19.

(4) S. L. Brock and S. M. Kauzlarich, Structure-property relationships in a series of mixed layer pnictide oxide compounds: $A_2Mn_3Pn_2O_2$ (A Sr, Ba; PnP, As, Sb), *J. Alloys Compd.*, **1996**, *241*, 82–88.

(5) Pöttgen, R.; Johrendt, D. Materials with ZrCuSiAs-type Structure, Z. Naturforsch. B. **2008**, *63*, 1135-1148.

(6) Muir, S.; Subramanian, M. A. ZrCuSiAs type layered oxypnictides: A bird's eye view of LnMPnO compositions, *Prog. Solid State Chem.* **2012**, *40*, 41-56.

(7) Just, G.; Paufler, P.On the coordination of $ThCr_2Si_2$ ($BaAl_4$)-type compounds within the field of free parameters, *J. Alloys Compd.* **1996**, *232*, 1-25.

(8) Belsky, A.; Hellenbrandt, M.; Karen, V. L.; Luksch, P. New developments in the Inorganic Crystal Structure Database (ICSD): accessibility in support of materials research and design, *Acta Crystallogr. Sect B: Structural Science* **2002**, *58*, 364-369.

(9) Brock, S. L.; Kauzlarich, S. M. $A_2Zn_3As_2O_2$ (A = Ba, Sr): A Rare Example of Square Planar Zinc*Inorg. Chem.*, **1994**, *33*, 2491–2492.

(10) Ozawa, T.; Olmstead, M. M.; Brock, S. L.; Kauzlarich, S. M.; Young, D. M., Synthesis and Characterization of a New Compound with Alternating MnO_2^{2-} and $Zn_2As_2^{2-}$ Layers: $Ba_2MnZn_2As_2O_2$, *Chem. Mater.*, **1998**, *10*, 392–396.

(11) Ozawa, T. C.; Kauzlarich, S. M.; Bieringer, M.; Wiebe, C. R.; Greedan, J. E.; Gardner, J. S. The Effect of Interlayer Cations on the Magnetic Properties of the Mixed-Metal Pnictide Oxides: $A_2MnZn_2As_2O_2$ (A = Sr, Ba), *Chem. Mater.*, **2001**, *13*, 973–980.

(12) Jiang, H.; Bao, J.-K.; Zhai, H.-F.; Tang, Z.-T.; Sun, Y.-L.; Liu, Y.; Wang, Z.-C.; Bai, Z.-C.; Xu, Z.-A.; Cao, G.-H., Physical properties and electronic structure of $Sr_2Cr_3As_2O_2$ containing CrO_2 and Cr_2As_2 square-planar lattices, *Phys. Rev. B*, **2015**, *92*, 205107

(13) Liu, J.; Wang, J.; Sheng, J.; Ye, F.; Taddei, K. M.; Fernandez-Baca, J. A.; Luo, W.; Sun, G.-A.; Wang, Z.-C.; Jiang, H.; Cao, G.-H.; Bao, W. Neutron diffraction study on magnetic structures and transitions in $Sr_2Cr_3As_2O_2$, *Phys. Rev. B* **2018**, *98*, 134416.

(14) Ozawa, T. C.; Kauzlarich, S. M. Chemistry of layered d-metal pnictide oxides and their potential as candidates for new superconductors, *Sci. Technol. Adv. Mater.* **2008**, *9*, 033003.

(15) Clarke, S. J.; Adamson, P.; Herkelrath, S. J. C.; Rutt, O. J.; Parker, D. R.; Pitcher, M. J.; Smura, C. F. Structures, Physical Properties, and Chemistry of Layered Oxychalcogenides and Oxypnictides. *Inorg. Chem.* **2008**, *47*, 8473-8486.

(16) Hayward, M. A. Synthesis and Magnetism of Extended Solids Containing Transition-Metal Cations in Square-Planar, MO_4 Coordination Sites, *Inorg. Chem.* **2019**, *58*, 11961-11970.

(17) Singh, Y.; Green, M. A.; Huang, Q.; Kreyssig, A.; McQueeney, R. J.; Johnston, D. C.; Goldman, A. I. Magnetic order in $BaMn_2As_2$ from neutron diffraction measurements, *Phys. Rev. B*, **2009**, *80*, 100403(R).

(18) Emery, N.; Wildman, E. J.; Skakle, J. M. S.; Mclaughlin, A. C.; Smith, R. I.; Fitch, A. N. Variable temperature study of the crystal and magnetic structures of the giant magnetoresistant materials LMnAsO(L = La, Nd) *Phys. Rev. B*, **2011**, *83*, 144429.

(19) Marcinkova, A.; Hansen, T. C.; Curfs, C.; Margadonna, S.; Bos, J. W. G., Nd-induced Mn spin-reorientation transition in NdMnAsO, *Phys. Rev. B* **2010**, *82*, 174438.

(20) Corkett, A. J.; Free, D. G.; Clarke, S. J., Spin-Reorientation Transition in CeMnAsO, *Inorg. Chem.*, **2015**, *54*, 1178–1184.

(21) Enjalran, M.; Scalettar, R. T.; Kauzlarich, S. M., Magnetic states in frustrated bilayer models: The ordered phase of mixed-layer pnictide oxides, *Phys Rev. B* **2000**, *61*, 14570–14580.

(22) Nath, R.; Garlea, V. O.; Goldman, A. I.; Johnston, D. C., Synthesis, structure, and properties of tetragonal $Sr_2M_3As_2O_2$ (M_3 =Mn_3, Mn_2Cu, and $MnZn_2$) compounds containing alternating CuO_2-type and FeAs-type layers, *Phys. Rev. B* **2010**, *81*, 224513.

(23) An, J.; Sefat, A. S.; Singh, D. J.; Du, M-H. Electronic structure and magnetism in $BaMn_2As_2$ and $BaMn_2Sb_2$ *Phys. Rev. B.***2009**, *79*, 075120.

(24) Singh, Y.; Ellern, A.; Johnston, D. C., Magnetic, transport, and thermal properties of single crystals of the layered arsenide $BaMn_2As_2$, *Phys. Rev. B,* **2009**, *79*, 094519.

(25) Tsukamoto, Y.; Okamoto, Y.; Matsuhira, K.; Whangbo, M.-H.; Hiroi, Z., A Magnetic Transition Probed by the Ce Ion in Square-Lattice Antiferromagnet CeMnAsO, *J. Phys. Soc. Jpn* **2011** *80,* 094708.

(26) Eguchi, N.; Ishikawa, F.; Kodama, M.; Wakabayashi, T.; Nakayama, A.; Ohmura, A.; Yamada, Y., Synthesis of New Layered Oxypnictides $Sr_2CrO_2(FeAs)_2$, *J. Phys Soc. Jpn*, **2013**, *82*, 045002.

(27) Yuzuri, M., On the Magnetic Properties of Cr_2As and Cu_2Sb *J. Phys. Soc. Jpn*. **1960**, *15*, 2007.

(28) Park, S.-W.; Mizoguchi, H.; Kodama, K.; Shamoto, S.; Otomo, T.; Matsuishi, S.; Kamiya, T.; Hosono, H., Magnetic Structure and Electromagnetic Properties of LnCrAsO with a ZrCuSiAs-type Structure (Ln = La, Ce, Pr, and Nd), *Inorg. Chem.*, **2013**, *52*, 13363–13368.

(29) Singh, D. J.; Sefat, A. S.; McGuire, M. A.; Sales, B. C.; Mandrus, D.; VanBebber, L. H.; Keppens, V., Itinerant antiferromagnetism in $BaCr_2As_2$: Experimental characterization and electronic structure calculations*Phys. Rev. B*, **2009**, *79*, 094429.

(30) Filsinger, K. A.; Schnelle, W.; Adler, P.; Fecher, G. H.; Reehuis, M.; Hoser, A.; Hoffmann, J.-U.; Werner, P.; Greenblatt, M; Felser, C. Antiferromagnetic structure and electronic properties of $BaCr_2As_2$ and $BaCrFeAs_2$ *Phys. Rev. B* **2017**, *95*, 184414

(31) Thompson, S. P.; Parker, J. E.; Potter. J.; Hill, T. P.; Birt, A.; Cobb, T. M.; Yuan, F.; Tang, C. C. *Review of Scientific Instruments* **2009**, *80*, 075107.

(32) Chapon, L. C.; Manuel, P.; Radaelli, P. G.; Benson, C.; Perrott, L.; Ansell, S.; Rhodes, N. J.; Raspino, D.; Duxbury, D.; Spill, E.; Norris, J. WISH: The New Powder and Single Crystal Magnetic Diffractometer on the Second Target Station. *Neutron News* **2011**, *22*, 22–25.

(33) Coelho, A. A. *TOPAS academic: General profile and Structure Analysis Software For Powder Diffraction Data*; Bruker AXS; Karlsurhe, Germany, **2012**.

(34) Campbell, B. J.; Stokes, H. T.; Tanner, D. E.; Hatch, D. M. ISODISPLACE: a web-based tool for exploring structural distortions. *J. Appl. Crystallogr.* **2006**, *39*, 607-614.

(35) Shirane, G., A note on the magnetic intensities of powder neutron diffraction, *Acta Crystallogr.* **1959**, *12*, 282-285.

(36) Zhu, W. J.; Hor, P. H. Synthesis and Structure of Layered Manganese Oxychalcogenides: Sr_2CuMnO_3S and $Sr_4Cu_2Mn_3O_{7.5}Q_2$ (Q = S, Se), *J. Solid State Chem.* **2000**, *153*, 26-29.

(37) Shannon, R. D. *Acta Crystallogr.,* **1976**, *A32*, 751-767.

(38) von Schnering, H. G. and Brand, B.-H. Struktur und Eigenschaften des blauen Chrom(II)-chlorid-tetrahydrats $CrCl_2 . 4H_2O$, *Z. Anorg. Allg. Chem.* **1973**, *402*, 159-168.

(39) Somer, M.; Carrillo Cabrera, W.; Peters, K.; von Schnering, H. G., Crystal structure of tetrastrontium triarsenide, Sr_4As_3, *Z. Kristallogr.*, **1995**, *210*, 876-876.

(40) Brauer G. and Müller, O., Zur Kristallchemie des Strontiumchlorids, *Z. Anorg. Allg. Chem.* **1958**, *295*, 218-226.

(41) Howard, C. J.; Kennedy, B. J.; Curfs, C., Temperature-induced structural changes in $CaCl_2$,$CaBr_2$, and $CrCl_2$: A synchrotron x-ray powder diffraction study, *Phys. Rev. B* **2005**, *72*, 214114.

(42) Whangbo, M.-H.; Gordon, E. E.; Xiang, H.; Koo, H.-J.; Lee, C. Prediction of Spin Orientations in Terms of HOMO−LUMO Interactions Using Spin−Orbit Coupling as Perturbation. *Acc. Chem. Res.* **2015**, *48*, 3080−3087.

(43) Senff, D.; Reutler, P.; Braden, M.; Friedt, O.; Bruns, D.; Cousson, A.; Bourée, F.; Merz, M.; Büchner, B.; Revcolevschi, A., Crystal and magnetic structure of $La_{1-x}Sr_{1+x}MnO_4$: Role of the orbital degree of freedom, *Phys. Rev. B* **2005** *71*, 024425.

(44) Qureshi, N.; Ulbrich, H.; Sidis, Y.; Cousson, A.; Braden, M., Magnetic structure and magnon dispersion in $LaSrFeO_4$, *Phys. Rev. B* **2013** *87*, 054433.

(45) Qureshi, N.; Valldor, M.; Weber, L.; Senyshyn, A.; Sidis, Y.; Braden, M., Magnetic spin-flop transition and interlayer spin-wave dispersion in $PrCaFeO_4$ revealed by neutron diffraction and inelastic neutron scattering, *Phys. Rev. B* **2015**, *91*, 224402.

(46) Oyama, S.; Wakeshima, M.; Hinatsu, Y.; Ohoyama, K.; Spin reorientation transition in layered perovskite $CaNdFeO_4$, *J. Phys.: Condens. Matter* **2004**, *16*, 8429–8446.

(47) Kimber, S. A. J.; Hill, A. H.; Zhang, Y.-Z.; Jeschke, H. O.; Valentí, R.; Ritter, C.; Schellenberg, I.; Hermes, W.; Pöttgen, R.; Argyriou, D. N. Local moments and symmetry breaking in metallic PrMnSbO, *Phys. Rev. B* **2010**, *82*, 100412(R).

(48) D. Dai, H. Xiang, M.-H. Whangbo, Effects of Spin-Orbit Coupling on Magnetic Properties of Discrete and Extended Magnetic Systems, Journal of Computational Chemistry, **2008**, *29*, 2187–2209.

(49) Mayer, J. M.; Schneemeyer, L. F.; Siegrist, T.; Waszczak, J. V.; Van Dover, B. New Layered Iron-Lanthanum-Oxide-Sulfide and -Selenide Phases: $Fe_2La_2O_3E_2$ (E= S,Se). *Angew. Chemie Int. Ed. English* **1992**, *31*, 1645–1647.

(50) Kabbour, H.; Janod, E.; Corraze, B.; Danot, M.; Lee, C.; Whangbo, M.-H.; Cario, L. Structure and Magnetic Properties of Oxychalcogenides $A_2F_2Fe_2OQ_2$ (A = Sr, Ba; Q = S, Se) with Fe_2O Square Planar Layers Representing an Antiferromagnetic Checkerboard Spin Lattice. *J. Am. Chem. Soc.* **2008**, *130*, 8261–8270.

(51) He, J. B.; Wang, D. M.; Shi, H. L.; Yang, H. X.; Li, J. Q.; Chen, G. F. Synthesis, structure, and magnetic properties of the layered iron oxychalcogenide $Na_2Fe_2Se_2O$. *Phys. Rev. B* **2011**, *84*, 205212.

(52) Takeiri, F.; Matsumoto, Y.; Yamamoto, T.; Hayashi, N.; Li, Z.; Tohyama, T.; Tassel, C.; Ritter, C.; Narumi, Y.; Hagiwara, M.; Kageyama, H., High-pressure synthesis of the layered iron oxyselenide $BaFe_2Se_2O$ with strong magnetic anisotropy. *Phys. Rev. B* **2016**, *94*, 184426.

(53) Zhang, Q; Kumar, C. M. N.; Tian, W.; Dennis, K. W.; Goldman, A. I.; Vaknin, D. Structure and magnetic properties of *Ln*MnSbO (*Ln* = La and Ce), *Phys. Rev. B* **2016**, *93*, 094413.

(54) Lawrence, G. B.; Wildman, E. J.; Stenning, G. B. G.; Ritter, C.; Fauth, F; Mclaughlin, A. C. Electronic and Magnetic Properties of Cation Ordered $Sr_2Mn_{2.23}Cr_{0.77}As_2O_2$, *Inorg. Chem.* **2020**, *59*, 7553–7560.

For Table of Contents Only

$Sr_2CrO_2Cr_2As_2$ and $Ba_2CrO_2Cr_2As_2$ display different complex magnetic ordering over two Cr^{2+} sublattices which is probed using high resolution diffraction.

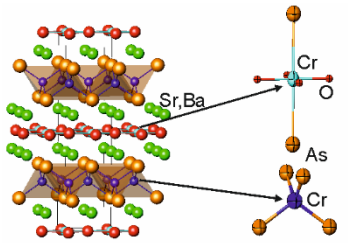

Supporting Information

Magnetic ordering in the layered Cr(II) oxide arsenides $Sr_2CrO_2Cr_2As_2$ and $Ba_2CrO_2Cr_2As_2$

Xiaoyu Xu,[1] Michael A. Jones,[1] Simon J Cassidy,[1] Pascal Manuel,[2] Fabio Orlandi,[2] Maria Batuk,[3] Joke Hadermann[3] and Simon J Clarke[1*]

[1]Department of Chemistry, University of Oxford, Inorganic Chemistry Laboratory, South Parks Road, Oxford, OX1 3QR, UK. [2]ISIS Facility, STFC Rutherford Appleton Laboratory, Harwell Oxford, Didcot OX11 0QX, United Kingdom. [3]Electron Microscopy for Materials Science (EMAT), University of Antwerp, Groenenborgerlaan 171, B-2020 Antwerp, Belgium.

email: simon.clarke@chem.ox.ac.uk

Table S1 Refinement results for $Sr_2CrO_2Cr_2As_2$ corresponding to the fits shown in Figures 2(a) and S4 (100 K).

Instrument	I11	I11	WISH
Radiation	X-ray	X-ray	Neutron
Wavelength (Å)	0.825901	0.825901	white beam
Temperature (K)	298	100K	623
R_{wp}	7.90	9.72	3.51
χ^2	2.22	1.54	0.77
Space group	*I*4/*mmm*	*I*4/*mmm*	*I*4/*mmm*
a (Å)	4.00800(2)	4.00273(2)	4.03128(7)
c (Å)	18.8214(1)	18.7204(1)	19.0399(4)
V (Å^3)	302.347(4)	299.934(4)	309.42(1)
ρ (g cm^{-3})	5.63573(8)	5.68107(8)	5.5069(2)
Cr(1)–O (Å) [4]	2.00400(1)	2.00136(1)	2.01564(4)
Cr(1)–As (Å) [2]	3.2072(7)	3.1835(8)	3.2391(6)
Cr(2)–As (Å) [4]	2.5021(4)	2.4990(5)	2.5251(3)
Sr–O (Å) [4]	2.5964(5)	2.5900(5)	2.6228(4)
Sr–As (Å) [4]	3.2333(5)	3.2220(5)	3.2499(4)
As–Cr–As (°) [2]	106.44(3)	106.42(3)	105.93(2)
As–Cr–As (°) [4]	111.01(1)	111.02(2)	111.27(1)

Table S2. Structural parameters for $Sr_2CrO_2Cr_2As_2$ from Rietveld refinement against I11 RT data (Figure 2(a))

atom	site	*x*	*y*	*z*	U_{11} / U_{22} (Å^2)[a]	U_{33} (Å^2)
Sr	4*e*	0	0	0.41229(4)	0.0107(3)	0.0133(5)
Cr(1)	2*a*	0	0	0	0.0098(5)	0.015(1)
Cr(2)	4*d*	0	0.5	0.25	0.0126(4)	0.0098(6)
As	4*e*	0	0	0.17040(4)	0.0155(3)	0.0165(5)
O	4*c*	0	0.5	0	0.004(1)[b]	0.004(1)[b]

[a] $U_{11} = U_{22}$ by symmetry for sites refined anisotropically.
[b] O atoms refined isotropically

Table S3. Structural parameters for $Sr_2CrO_2Cr_2As_2$ from Rietveld refinement against I11 100 K data (Figure S4).

atom	site	*x*	*y*	*z*	U_{11} / U_{22} (Å^2)[a]	U_{33} (Å^2)
Sr	4*e*	0	0	0.41218(4)	0.0066(3)	0.011(5)
Cr(1)	2*a*	0	0	0	0.0043(5)	0.0066(9)
Cr(2)	4*d*	0	0.5	0.25	0.0083(4)	0.0028(6)
As	4*e*	0	0	0.17006(4)	0.0090(3)	0.0127(5)
O	4*c*	0	0.5	0	0.0005(9)[b]	0.0005(9)[b]

[a] $U_{11} = U_{22}$ by symmetry for sites refined anisotropically.
[b] O atoms refined isotropically

Table S4. Structural parameters for $Sr_2CrO_2Cr_2As_2$ from Rietveld refinement against WISH 623K data (Figure 2(b)).

atom	site	*x*	*y*	*z*	U_{11} / U_{22} (Å^2)[a]	U_{33} (Å^2)
Sr	4*e*	0	0	0.41192(3)	0.0327(7)	0.079(1)
Cr(1)	2*a*	0	0	0	0.061(2)	0.032(3)
Cr(2)	4*d*	0	0.5	0.25	0.073(2)	0.006(2)
As	4*e*	0	0	0.17023(3)	0.0348(7)	0.059(1)
O	4*c*	0	0.5	0	0.0294(9) / 0.0210(9)	0.023(1)

[a] $U_{11} = U_{22}$ by symmetry except for 4*c* site

Table S5. Structural parameters for $Ba_2CrO_2Cr_2As_2$ from Rietveld Refinement against powder X-ray data (Table 1; Figure 2(c)).

Atom	Site	*x*	*y*	*z*	U_{11} / U_{22} (Å^2)[a]	U_{33} (Å^2)
Ba	4*e*	0	0	0.41073(2)	0.0149(2)	0.0161(3)
Cr(1)	2*a*	0	0	0	0.0090(6)	0.018(1)
Cr(2)	4*d*	0	0.5	0.25	0.0176(5)	0.0199(8)
As	4*e*	0	0	0.17813(4)	0.0152(4)	0.0189(6)
O	4*c*	0	0.5	0	0.010(2)[b]	0.010(2)[b]

[a] $U_{11} = U_{22}$ by symmetry for sites refined anisotropically.
[b] O atoms refined isotropically

Table S6. Structure parameters for $Ba_2CrO_2Cr_2As_2$ from Rietveld refinement against WISH NPD data at 473 K (Table 1; Figure 2(d)).

Atom	Site	*x*	*y*	*z*	U_{11} / U_{22}(Å^2)[a]	U_{33} (Å^2)
Ba	4*e*	0	0	0.41080(5)	0.0056(8)	0.005(1)
Cr(1)	2*a*	0	0	0	0.034(2)	0.002(2)
Cr(2)	4*d*	0	0.5	0.25	0.023(1)	0.052(2)
As	4*e*	0	0	0.17869(4)	0.0215(7)	0.028(1)
O	4c	0	0.5	0	0.010(1)/ 0.017(1)	0.013(1)

[a] $U_{11} = U_{22}$ by symmetry except for 4*c* site

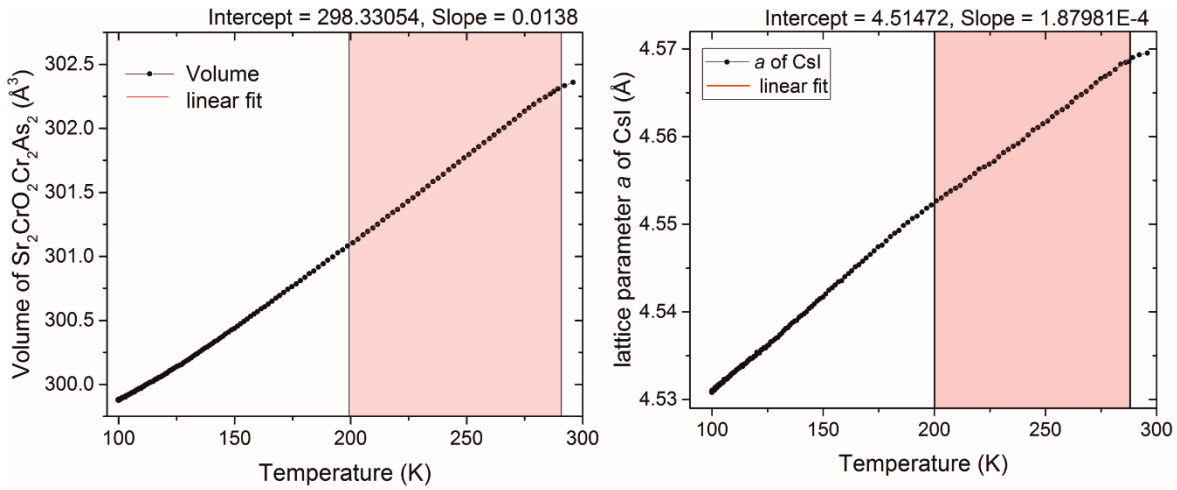

Figure S1. Temperature evolution of cell volume for $Sr_2CrO_2Cr_2As_2$ and the lattice parameter of the remanent CsI flux measured on I11.

Table S7. Calibration of the cryostat temperatures close to ambient temperatures in the PND measurements on WISH for sample 1 based on the behaviour in Figure S1.

Nominal Temperature (K)	CsI lattice parameter (Å)	Temperature calibrated by *a* CsI	$Sr_2CrO_2Cr_2As_2$ volume (Å^3)	Temperature calibrated by volume	average calibrated temperature
297 K / furnace unheated	4.5724	-	303.48	-	-
"296-310" K / cryostat	4.5690	278 K	303.28	282 K	280 K
"315-317" K / cryostat	4.5713	291 K	303.37	289 K	290 K
307 K / furnace	4.5743	307 K	303.652	309 K	308 K

The temperatures around ambient temperature measured in the cryostat used for some of the variable temperature PND measurements were overestimates of the true sample temperatures based on the behaviour of the lattice parameters of both the main phase and the minority CsI phase present as a remnant from the flux used in the synthesis.

Table S8. To examine the possible reduction of symmetry (see text), the magnetic only reflections of the neutron diffraction pattern of $Sr_2CrO_2Cr_2As_2$ were fit using the model-independent Pawley while the nuclear reflections were modelled with a structural model by the Rietveld method. The *c* lattice parameter of the magnetic unit cell was fixed equal to the *c* parameter of the nuclear cell. The *a* and *b* cell parameters of the magnetic cell were either fixed to √2 expansion of the nuclear *a* cell parameter or each allowed to refine independently. The corresponding lattice parameters for the magnetic phase and agreement factors for the fit to all 5 detector banks are given. The improvement in R_{wp} is also depicted in Figure S2.

Temperature (K)	tetragonal *a* parameter (Å)	R_{wp} (%)	orthorhombic *a* parameter (Å)	orthorhombic *b* parameter (Å)	R_{wp} (%)
1.5	5.66604(5)	4.26	5.6610(2)	5.6699(2)	3.54
100	5.66676(5)	4.23	5.6615(2)	5.6708(2)	3.60
150	5.66789(9)	4.24	5.6629(2)	5.6719(2)	3.68
200	5.67042(5)	4.03	5.6647(2)	5.6741(2)	3.54
247	5.67169(5)	3.79	5.6663(2)	5.6747(2)	3.43
280	5.67350(7)	3.81	5.6694(2)	5.6772(2)	3.61
290	5.67375(9)	3.46	5.6737(3)	5.6738(3)	3.45

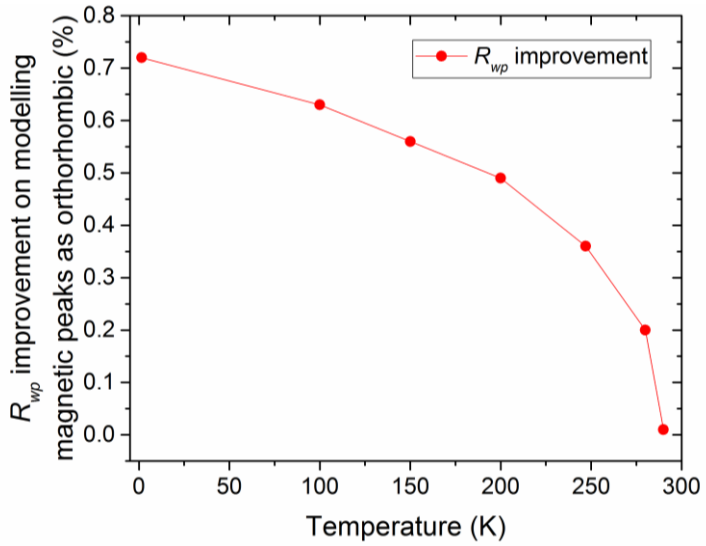

Figure S2. Improvement of the agreement factor on modelling the magnetic reflections in the neutron diffraction pattern with an orthorhombic Pawley phase instead of a tetragonal Pawley phase. See also Table S8.

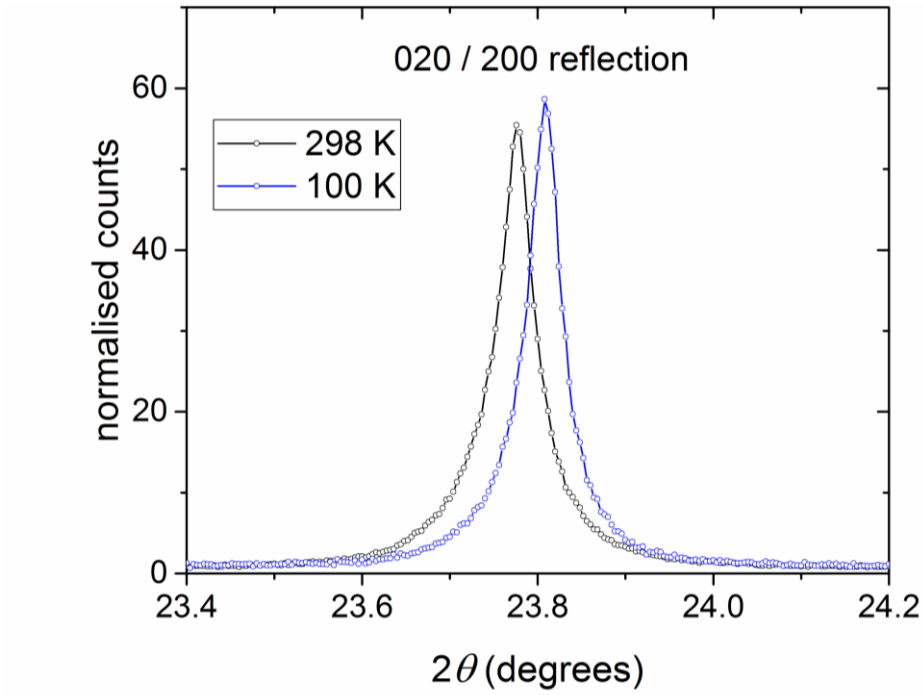

Figure S3. High resolution powder diffraction patterns comparing the 200 peak of tetragonal $Sr_2CrO_2Cr_2As_2$ at ambient temperature and 100 K, both collected using the MAC detector of beamline I11 at diamond light source. The data show no evidence of the nuclear unit cell undergoing an orthorhombic distortion.

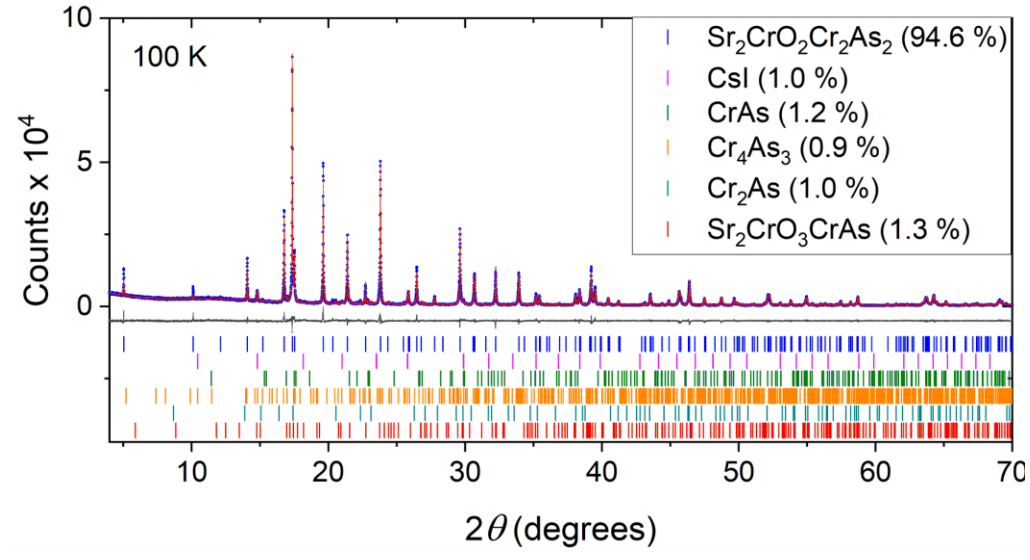

Figure S4. Rietveld refinements of the nuclear structure of $Sr_2CrO_2Cr_2As_2$ against synchrotron PXRD data (I11) collected at 100 K. See Tables S1, S3.

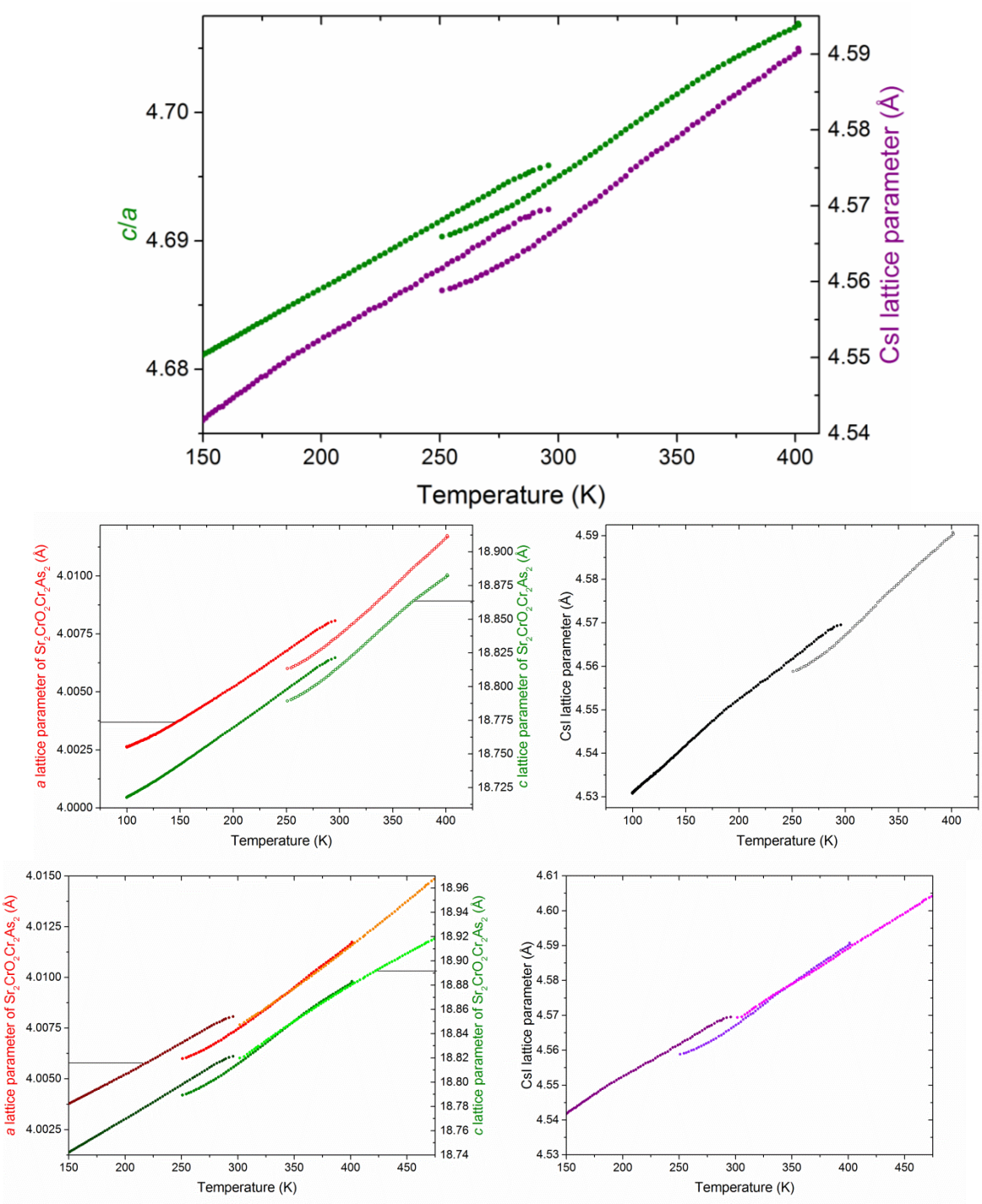

Figure S5. Figures showing evolution of the lattice parameters of $Sr_2CrO_2Cr_2As_2$ and the minor CsI impurity as a function of temperature. Three temperature sweeps with overlapping temperature ranges were used. The behaviour of the lattice parameter of the CsI impurity which is used as an internal standard matches that of the lattice parameters of the main phase showing that the curvature in the lattice parameter vs temperature plots at the extremities of some of the temperature sweeps, and the relative offsets of the different sweeps are artifacts of the way the temperature sweeps were performed. No genuine discontinuous changes in lattice parameters are observed for $Sr_2CrO_2Cr_2As_2$ as a function of temperature.

Magnetic symmetry analysis of $Sr_2CrO_2Cr_2As_2$ spin reorientation (See Figures S6 & S7).

Using the Isotropy suite[1] we derived the magnetic symmetry of the system to gather some insights into the possible type of coupling between the two Cr sub-lattices. It is important to underline that the two sub-lattices order with two different propagation vectors indicating that, in first instance, they are not coupled one to the other, which is in agreement with the two different ordering temperatures and the 90 degree orientation between them. However, the solid experimental evidence of the common spin reorientation transition suggests the presence of some sort of coupling.

The Cr(2) sub-lattice orders with the propagation vector k_1= (1 1 1) corresponding to the M point of the first Brillouin zone, a violation of the nuclear *I* centring symmetry. The AFM solution with the spins perpendicular to the plane transforms as the mM_4^+ irreducible representation (Irrep) with order parameter P(α) corresponds to the P_I4_2/mnm magnetic space group described in the same cell as the parent $I4/mmm$ structure. Around RT the Cr(1) sub-lattice orders antiferromagnetically with the moments in plane with propagation vector k_2 = (½ ½ 0) and Irrep mX_3^+ with order parameter P(0, ϕ_2). As stated above there is no "direct" coupling between the two sub-lattices since they order with two different propagation vectors and therefore they transform as different magnetic Irreps. The only mechanism to couple these two orderings is through a nuclear distortion. Using group theory, we deduce that the only possible distortion that will couple the mM_4^+ and mX_3^+ irreps is the X_4^+ one. In the general case the invariant is written as follow:

$$\alpha(\phi_1\delta_2-\phi_2\delta_1)$$

where α, ϕ_i are the directions of the order parameter for the mM_4^+ (1D irreps) and mX_3^+ (2D irreps) respectively and δ_i are the order parameter directions for the nuclear X_4^+ distortion.

In our particular case the order parameter direction of the mX_3^+ magnetic distortion is (0, ϕ_2) that reduces the invariant to $\alpha\phi_2\delta_1$. This gives us some restriction on the order parameter direction of the nuclear distortion and in particular the best candidate is in the order parameter direction (δ_1,0). This distortion corresponds to a tilting of the chromium-oxygen square planar lattice together with an in-plane anti-polar distortion of the Sr and As atoms. This coupling is maintained also during the spin reorientation transition, where the symmetry is lowered to monoclinic P_C2_1/c due to the action of the mM_5^+ (in plane ordering of the Cr(2) sublattice) and of the mX_2^+ (out of plane ordering of the Cr(1) sub-lattice), and in the final ground state where the magnetic structure is described by the P_Cccn magnetic space group obtained from the action of the mM_5^+ and mX_2^+ magnetic Irreps (for more details see the graph in Figure S6).

The X_4^+ distortion can be present as secondary order parameter thanks to the common action of both mM_4^+ and mX_3^+ distortions (as also from the other magnetic Irreps at low T) so the coupling mechanism will be present in any case, but if the X_4^+ nuclear distortion is already present in the paramagnetic phase this will explain why the Cr1 orders with the k_2 propagation vector. Indeed the choice of the mX_3^+ Irreps for the magnetic order will allow the system to take advantage of the coupling already present in the system without the need to create a new nuclear distortion in order to couple to the magnetic sub-lattices. This symmetry analysis unfortunately does not clarify the microscopic mechanism that leads to the coupling between the two sub-lattices but only indicates the need of a nuclear distortion for the Dzyaloshinskii–Moriya interaction to operate [2] There is no evidence for the required distortion in our diffraction investigations. See main text for further discussion.

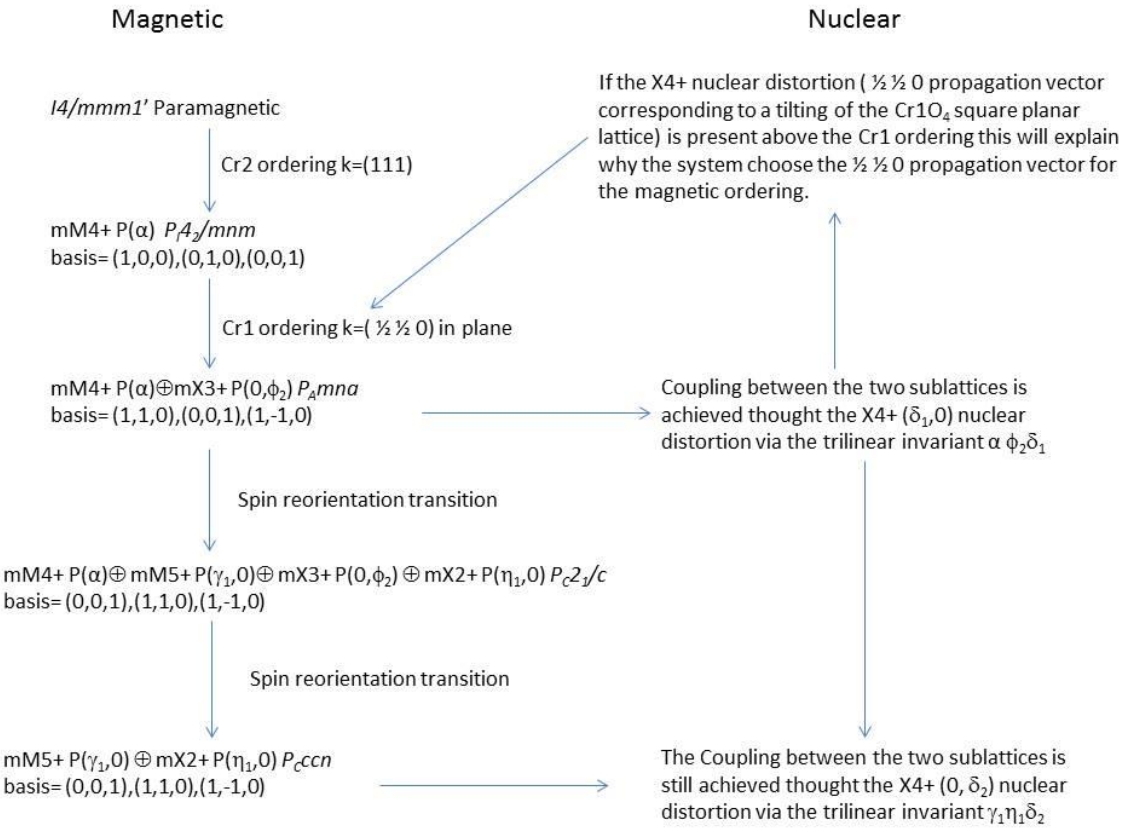

Figure S6. Graph showing the relations between the different magnetic and nuclear distortions and the relative coupling in $Sr_2CrO_2Cr_2As_2$ compound. The different magnetic structures and the relative magnetic space groups refers to Figure S7.

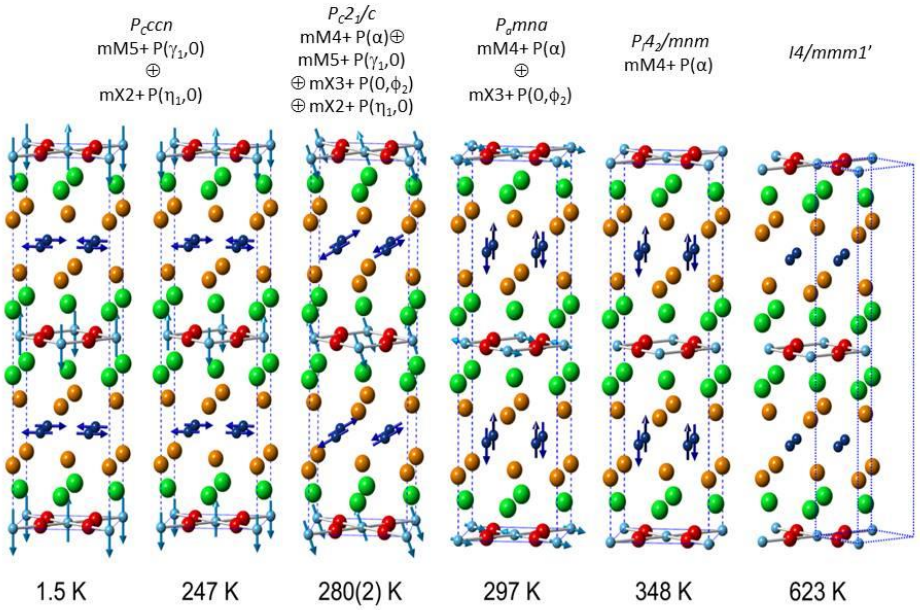

Figure S7. Schematic representation of the magnetic ordering and spin reorientation in $Sr_2CrO_2Cr_2As_2$. For each temperature is reported the magnetic space group and the relative irreducible representations and order parameters.

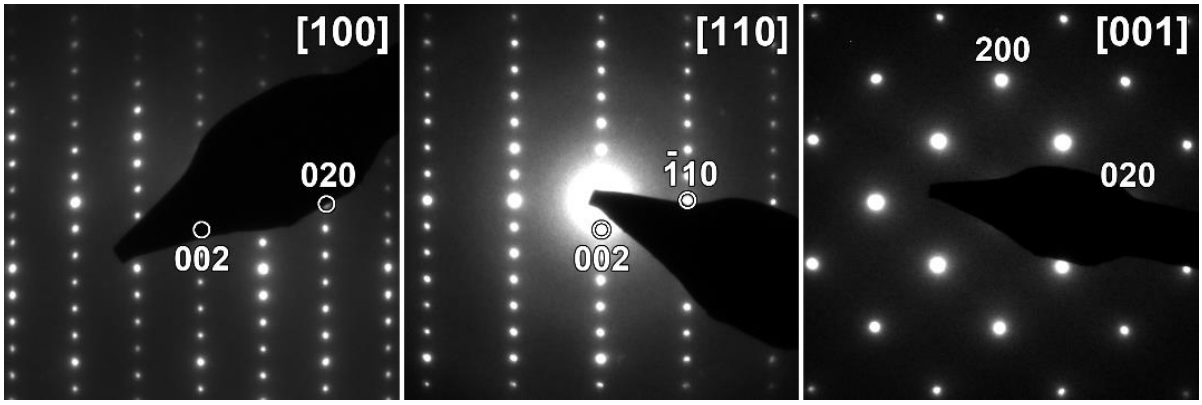

Figure S8. Electron diffraction patterns acquired at -175°C. No changes were observed in comparison to the room temperature patterns.

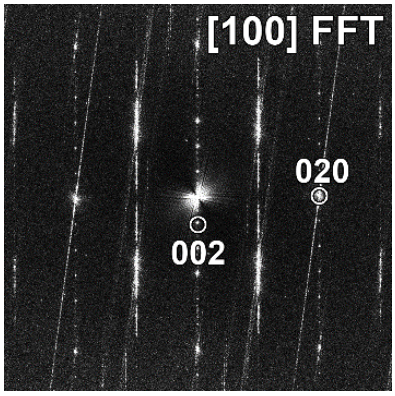

Figure S9. Fourier transform from the image in Figure 12(b) (main text). The rows of closely spaced reflections that can be seen along the c* axis, where in most [100] ED patterns only streaks are present, indicate that several ordering patterns are present between the stacking faults, that are coherent over large enough areas to result in Bragg reflections. This is further clarified in Figure S10.

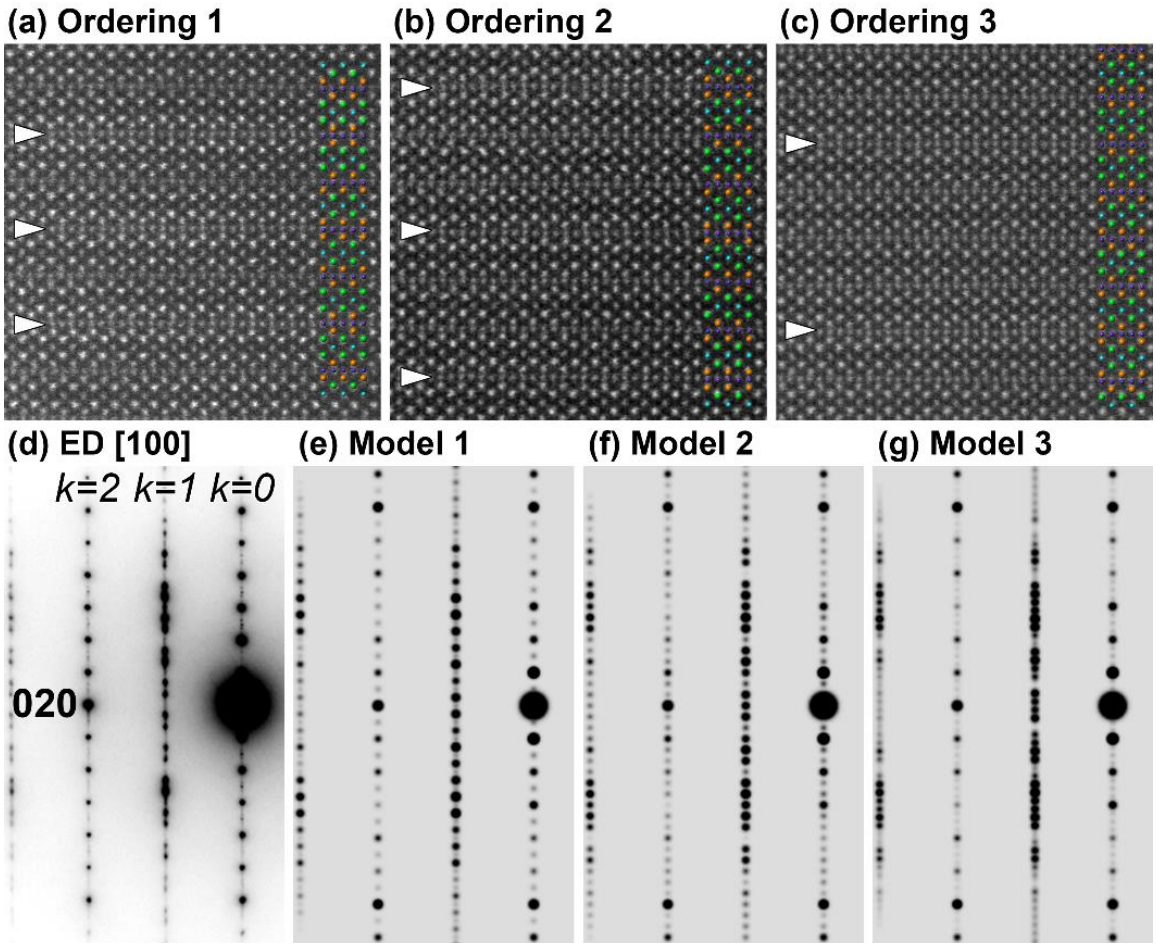

Figure S10. HAADF-STEM images showing parts of the crystal with different ordering of the stacking faults with model overlays (Sr – green; As – orange; Cr1 – turquoise; Cr2 – violet; oxygen atoms are not shown for clarity). The stacking faults are indicated with arrowheads (a-c). Experimental electron diffraction pattern showing additional reflections along the c* axis (d) and simulated patterns of the models 1-3 (e)-(g). The slight deviations between calculated and experimental patterns are caused by different ratios of the different orderings occurring, depending on the chose area.

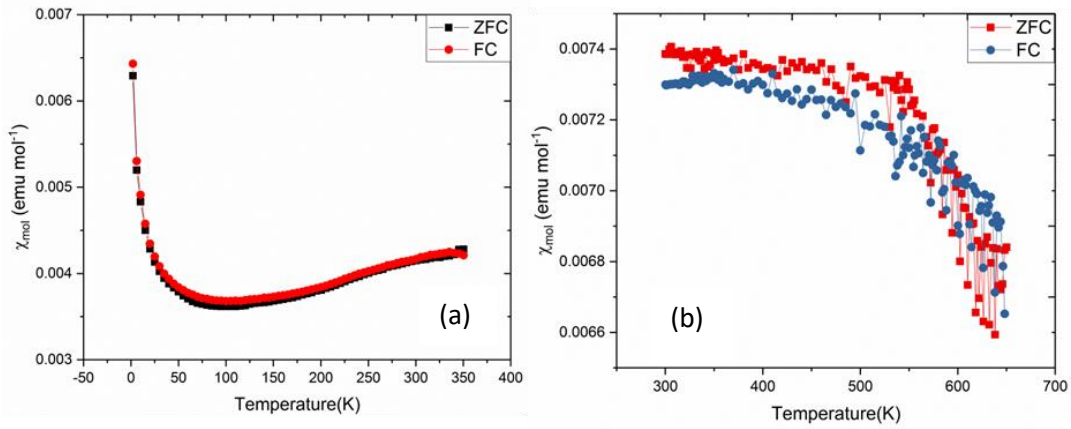

Figure S11. (a) SQUID magnetometry data for $Ba_2CrO_2Cr_2As_2$ at 1000 Oe between 2 K and 350 K; (b) High-temperature SQUID magnetometry data for $Ba_2CrO_2Cr_2As_2$ at 5000 Oe between 300 K and 650 K; The two data sets were collected using different sample environments.

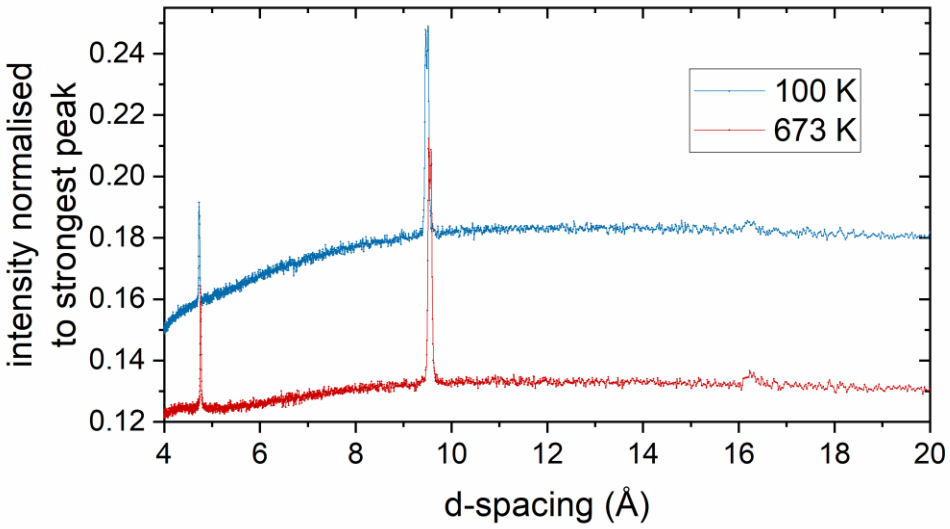

Figure S12. Portions of powder X-ray diffractograms of $Sr_2CrO_2Cr_2As_2$ measured on Instrument I11 at Diamond and plotted in *d*-spacing for comparison with main Figure 8. This figure shows that no extra scattering appears at 17 Å at low temperatures, in contrast to the neutron case (the peak at around 16Å is the 001 reflection of a minor impurity Sr_2CrO_3CrAs)

References.

1. Campbell, B. J.; Stokes, H. T.; Tanner, D. E.; Hatch, D. M. ISODISPLACE: An Internet Tool for Exploring Structural Distortions. *J. Appl. Crystallogr.* **2006**, *39*, 607-614.

2. Dzyaloshinskii, I. A thermodynamic theory of "weak" ferromagnetism of antiferromagnetics. *Journal of Physics and Chemistry of Solids*. **1958**, *4*, 241.